# Fault Geometry and Slip Distribution of the 2013 Mw 7.7 Balochistan Earthquake From Inversions of SAR and Optical Data

B. Lauer, R. Grandin, Y. Klinger

JGR Solid Earth

RESEARCH ARTICLE
10.1029/2019JB018380

# Fault Geometry and Slip Distribution of the 2013 Mw 7.7 Balochistan Earthquake From Inversions of SAR and Optical Data

B. Lauer[1], R. Grandin[1], and Y. Klinger[1]

[1]Institut de Physique du Globe de Paris, CNRS, Université de Paris, Paris, France

**Key Points:**
- The combination of radar and optical satellite data constrain fault geometry and slip distribution inversions
- Our modeling strategy combines a non-linear and a linear inversion that allow for modeling both the geometry and the slip distribution
- The large magnitude of the 2013 Mw 7.7 Balochistan earthquake explains the absence of shallow slip deficit for this earthquake

**Supporting Information:**
- Supporting Information S1

**Correspondence to:**
B. Lauer,
lauer@ipgp.fr

**Citation:**
Lauer, B., Grandin, R., & Klinger, Y. (2020). Fault geometry and slip distribution of the 2013 Mw 7.7 Balochistan earthquake from inversions of SAR and optical data. *Journal of Geophysical Research: Solid Earth*, *125*, e2019JB018380. https://doi.org/10.1029/2019JB018380

Received 14 JUL 2019
Accepted 6 JUN 2020
Accepted article online 10 JUN 2020

**Abstract** The 2013 Mw 7.7 Balochistan earthquake ruptured the Hoshab fault (Pakistan) over 200 km. It was dominated by left-lateral slip, with a secondary reverse component. By combining optical (SPOT 5 and Landsat 8) and radar satellite data (RADARSAT-2 and TerraSAR-X ScanSAR), we derive the 3-D coseismic displacement field and the slip distribution. Our modeling strategy involves two successive inversions allowing to explore first the fault geometry and then slip distribution. Following a statistical analysis of the coseismic surface trace, the fault is discretized into 16 segments. To determine the dip angle and down-dip width of the segments, we then perform a non-linear elastic inversion of the geodetic data set. Using output of this model, we prescribe the fault geometry and linearly invert for slip at depth with refined discretization. Results show a decrease of the fault dip, reaching 50° in the central part of the fault that structurally connects the two sub-vertical terminations dipping at >70°. The distribution of strike-slip forms a shallow continuous patch (0–8 km) that peaks at 12.7 m of slip near the epicenter. Reverse slip is distributed on several patches and becomes shallower near the southern termination, where it peaks at 5.7 m. Our model shows an absence of shallow slip deficit (SSD), as for other Mw 7.5 + strike-slip earthquakes elsewhere, hence suggesting that SSD is only found for lesser magnitude earthquakes. We speculate that moment magnitude is a key element in the occurrence of SSD.

## 1. Introduction

The Chaman-Ghazaband-Ornach-Nal en échelon strike-slip Fault System (CFS) is located along the eastern border of the Makran accretionary wedge and accommodates the ~15 mm/year sinistral motion between Eurasia and India (Byrne et al., 1992; Szeliga et al., 2012). The 24 September 2013 Mw 7.7 Balochistan earthquake was an unexpected earthquake in that it did not occur directly on the main plate boundary (Figure 1). The earthquake did not break this major north-south trending fault system, where it could have ruptured either the Ghazaband fault, where the M7.7 1935 Quetta earthquake occurred further North (Singh & Gupta, 1980) or the Ornach-Nal fault that connects further South with the triple junction between India, Eurasia and Arabia. Instead, the 2013 earthquake nucleated on the Hoshab fault. This fault lies at the southern end of the CFS and extends toward the SW toward the interior of the Makran accretionary wedge (Lawrence et al., 1981; Platt et al., 1988), in an area where no large continental historical earthquakes (Mw > 7) had previously been documented (Ambraseys & Bilham, 2003; Bilham et al., 2007).

The 2013 Balochistan earthquake propagated bilaterally, predominantly toward the south, with a minor northward propagation. The rupture indeed mainly propagated from the junction with the CFS, to the North, to a section where the fault strikes at ~45° angle with respect to the CFS, to the South (Figure 1). Coseismic motion was confined in the upper 10 km of the crust and was dominated by left-lateral slip (up to 11 m) with a secondary reverse slip component (Avouac et al., 2014; Barnhart et al., 2014; Barnhart et al., 2019; Jolivet et al., 2014; Vallage et al., 2015; Zhou et al., 2018; Zinke et al., 2014). The surface rupture shows a complex pattern with areas of partitioning (Barnhart et al., 2015), distributed deformation (Gold et al., 2015; Vallage et al., 2015; Zhou et al., 2015; Zinke et al., 2014) and several kilometric-scale complexities and bends (Vallage et al., 2016). Several along-strike geometries have been proposed for the fault dip (Avouac et al., 2014; Barnhart et al., 2014; Jolivet et al., 2014; Zhou et al., 2016). Dip angle variations along depth have also been suggested. With the help of high-resolution optical data from SPOT 5 satellite, Vallage et al. (2015) proposed that changes in the dip angle of the fault at shallow depth explain near-fault displacements (a few hundred meters from the fault trace), with a shallowing of the very top part the fault (upper

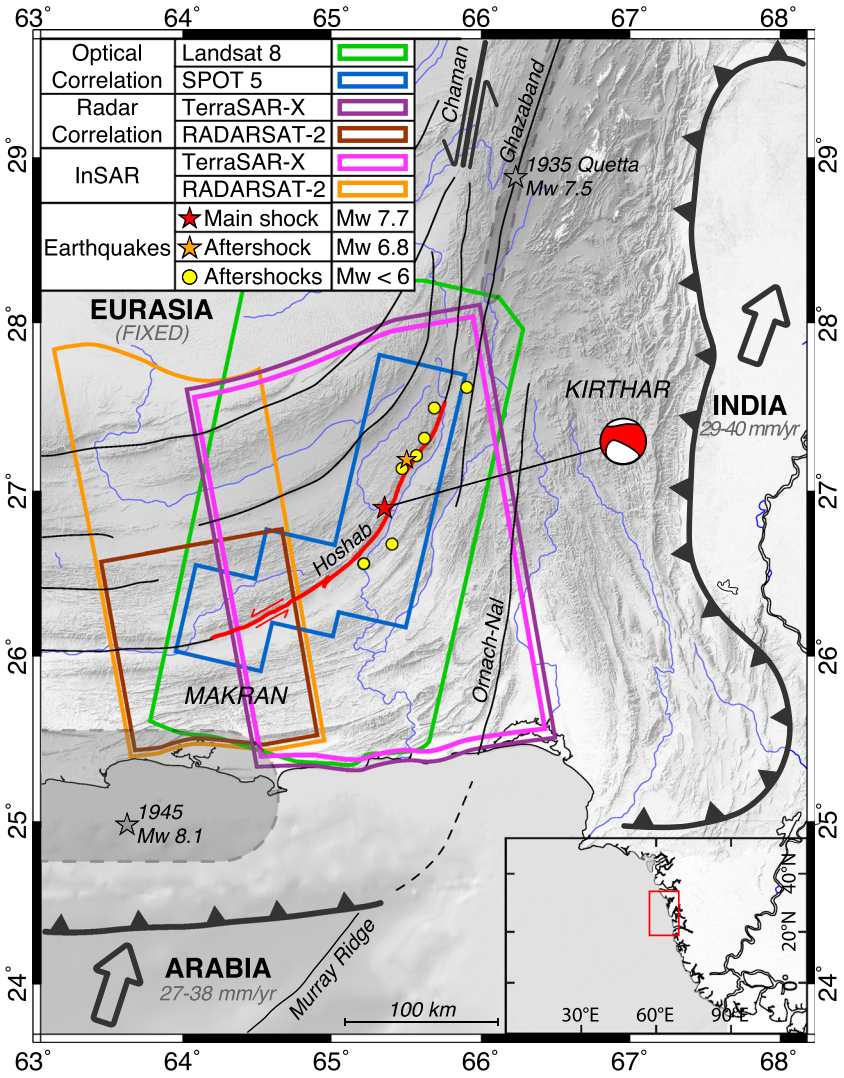


**Figure 1.** Seismotectonic setting of the Balochistan earthquake (24 September 2013, Mw 7.7). Boxes show the footprint of each data set. Fault trace from Vallage et al. (2016), epicenter from Barnhart et al. (2014), aftershock and historical seismicity (gray stars) epicenters from USGS, tectonic plates motion (relative to stable Eurasia) from Ader et al. (2012), DeMets et al. (2010), and Reilinger et al. (2006), tectonic setting based on Byrne et al. (1992), Kukowski et al. (2000), and Lawrence et al. (1981).

kilometer). However, the overall variability of the slip at depth and the fault geometry, especially its dip, are largely unconstrained due to the lack of observations on the vertical component of coseismic displacement.

In this study, we seek to measure the coseismic deformation in 3-D and determine the fault geometry for the Balochistan earthquake. In order to enhance the data coverage, we complement Landsat 8 optical data with high-resolution optical data from SPOT 5 satellite (Vallage et al., 2015). Unfortunately, due to the failure of ENVISAT and ALOS in 2012, the Balochistan earthquake was concordant with a period with a paucity of InSAR data. InSAR data indeed bring information on the far-field deformation pattern and allow for constraining processes that occur at depth. Here, we were able to process TerraSAR-X data in ScanSAR mode, along with already available RADARSAT-2 data. Combined with pixel offset tracking, these data allow for completely covering the whole rupture. We exploit this data set to derive the full 3-D coseismic displacement field at the surface.

SAR data and high-resolution optical correlation allow us to estimate the slip distribution of the earthquake, along with the 3-D geometry of the causative fault. Following a statistical analysis of the coseismic surface trace, the fault is discretized into 16 segments. To determine the geometry for these 16 segments, we

perform a non-linear elastic inversion, considering each segment as a single dislocation. We then use this first order model to set the geometry and linearly invert for slip and rake at depth with discretized segments.

We use these results to discuss several aspects. First, we address the question of the absence of shallow slip deficit for the Balochistan earthquake and compare this case to other major past strike-slip earthquakes. Second, we concentrate on the fault segmentation and the geometrical complexities that punctuate the rupture. From north to south, Vallage et al. (2015) highlighted two bends (b1 and b2), two relay zones (c1 and push-up c2), and one paired-bend (c3). Such complexities are visible in the morphology, and we seek to better understand their role in the rupture process and whether they influence the slip distribution.

## 2. Geodetic Data Set

The rich satellite imagery coverage of the 2013 earthquake rupture, combined with arid climatic conditions, offers an opportunity to investigate in detail surface ruptures and coseismic deformation. We use already published optical data from Landsat 8 and SPOT 5 by Vallage et al. (2015), and we processed SAR data from RADARSAT 2 and Terra-SAR X, leading to the first complete SAR coverage of this rupture. This data set allows us to span the whole rupture with multiple acquisition geometries. Metadata of all geodetic images are available in the supporting information Tables S1 to S4.

### 2.1. Optical Imagery

North-south and east-west components of coseismic motion are obtained by performing cross-correlation of pixels from two optical scenes: one before (master scene) and one after the earthquake (slave scene). We use offset fields derived from the correlation of five pairs of SPOT 5 satellite images and two pairs of Landsat 8 images (Vallage et al., 2015). Cross-correlation has been performed using the open-source software MicMac (Rosu et al., 2014), while co-registration and ortho-rectification have been done with COSI-Corr (Leprince et al., 2007). Landsat 8 offset field offers a pixel size of 15 m and has been corrected from residuals ramps and along-track striping due to the push-broom CCD sensor. SPOT 5 results give a ground pixel size of 2.5 m. With a limited footprint (60 × 60 km), SPOT 5 images are smaller than the earthquake displacement field (Figure 2). Offset values at the edges of SPOT 5 images are thus not null and cannot be taken as a reference in the post-processing steps. Since the Landsat 8 displacement field footprint is larger than the measurable surface displacements caused by the earthquake, Vallage et al. (2015) used Landsat 8 data as a proxy to estimate and correct for residual ramps in SPOT 5 data.

Both data sets cover the entire rupture area (Figure 2). The surface trace of the rupture is clearly visible in both NS and EW displacements, especially in SPOT 5 data. Maximum displacements are observed in the middle and southern parts of the rupture. Moreover, the displacement field is asymmetric across the fault, with more displacement affecting the block to the northwest side of the fault, indicating a NW dipping fault (Avouac et al., 2014; Barnhart et al., 2014; Gold et al., 2015; Jolivet et al., 2014; Vallage et al., 2015; Zhou et al., 2016; Zinke et al., 2014).

### 2.2. Radar Imagery

We used SAR data on one ascending track of RADARSAT 2 (C-band, 5.6 cm wavelength, Canadian Space Agency [CSA]) in stripmap mode and two tracks of TerraSAR-X/TanDEM-X (X-band, 3.1 cm wavelength, German Aerospace Center-DLR-Deutsches Zentrum für Luft-und Raumfahrt) in ScanSAR mode (Figure 3). RADARSAT-2 scenes are the same as Jolivet et al. (2014). Both RADARSAT-2 and TerraSAR-X images were acquired in an ascending orbit. Mean incidence angles in the part of the images affected by coseismic deformation are respectively 42° and 29°.

Differences in the phase of the radar waves returning to the satellite before and after the earthquake contain information about topography, satellite orbit, atmosphere, and deformation occurring between the two acquisitions (Massonnet & Feigl, 1998; Simons & Rosen, 2007). We generated coseismic interferograms by calculating the phase difference between the images acquired before and after the earthquake. The interferometric data were processed using the Caltech/JPL radar processing software ROI_PAC (Rosen et al., 2004). After corrections for topography using SRTM (Shuttle Radar Topography Mission) digital elevation model, interferograms were filtered, unwrapped, and referenced onto a geographic grid with a 115-m pixel size. The remaining phase difference is a measure of the ground displacement in the line of sight (LOS) to the satellite, with possible contributions of atmosphere and noise.

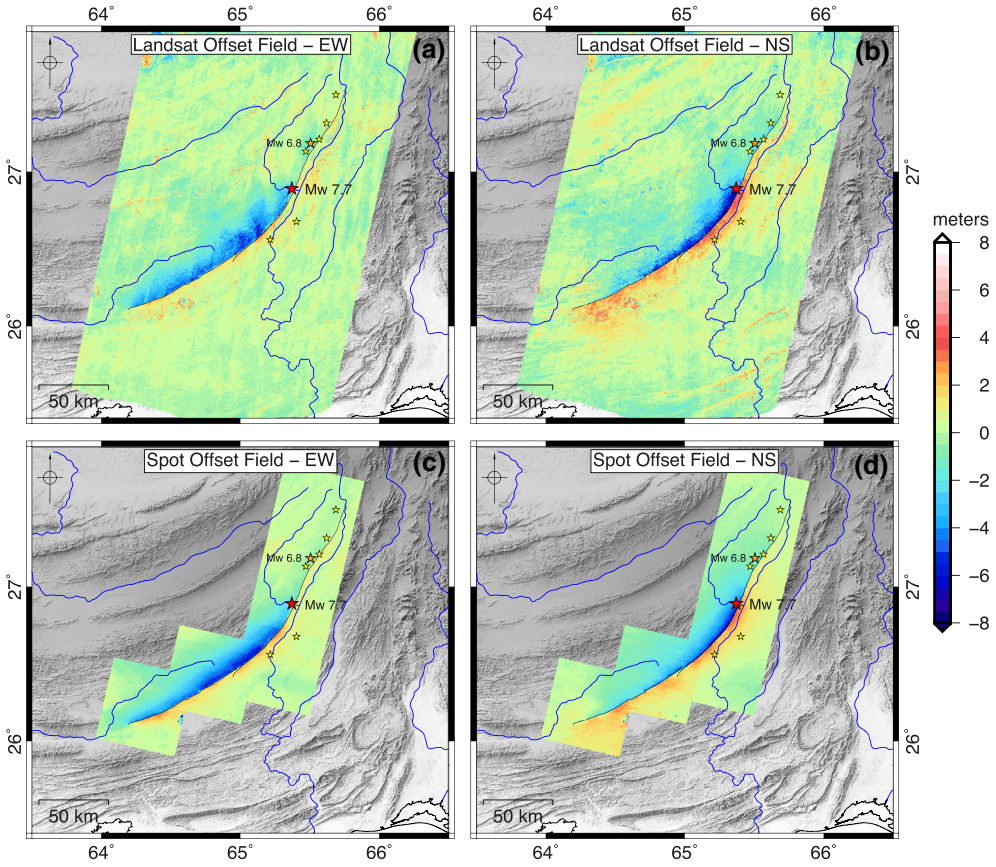


**Figure 2.** East-west and north-south displacement field (m) for the Balochistan earthquake measured from correlation of pre-earthquake and post-earthquake Landsat (a and b) and SPOT (c and d) optical images. Displacements are positive eastward (a and c) and northward (b and d). Data from Vallage et al. (2015), fault trace from Vallage et al. (2016), main shock epicenter from Barnhart et al. (2014), aftershock epicenters from USGS.

TerraSAR-X data acquired in ScanSAR mode required burst synchronization between the two acquisitions, which was achieved by DLR (Yague-Martinez et al., 2014). Images were first de-bursted in order to properly superimpose the successive bursts and produce a seamless image of the scene. Prior to interferogram generation, the azimuthally variable Doppler centroid frequency drift induced by the ScanSAR data mode was corrected using a deramping phase screen (Holzner & Bamler, 2002; Liang et al., 2013). The parameters of the quadratic phase term involved in the correction were initialized using the orbit information and refined using incoherent cross-correlation between master and slave amplitude images (Grandin, 2015).

We use a coherence-based unwrapper (Doin et al., 2011) that begins to unwrap the phase at a specific seed pixel. The algorithm progressively spreads the unwrapping, starting with regions of high coherence and then progressively decreases the coherence threshold. Since the western TerraSAR-X interferogram (scan 004) is cut in half by the fault zone (Figure 3b), we treated the data north and south of the fault separately. North of the fault, the fringes are continuous, and we manually made sure the fringes were consistent with the ones of the eastern interferogram (scan 008) that is continuous across both sides of the fault. South of the fault, the scan 004 interferogram is poorly coherent and shows a lot of isolated coherent zones. To take into account these isolated fringes that contain significant information, we manually added bridges to propagate the unwrapping beyond the discontinuities, assuming that phase varies smoothly across the gaps.

TerraSAR-X interferograms cover the central and northern parts of the rupture and RADARSAT-2 interferograms cover the southern extremity of the rupture (Figures 3a and 3b, rewrapped to a 24-cm color cycle). Phase decorrelation is observed on all interferograms near the fault where the coseismic displacement gradients are too large and where high surface damage and ground disruption occur. Our interferograms thus measure displacements in the far field (>10 km from the fault), showing up to 96 cm toward the satellite,

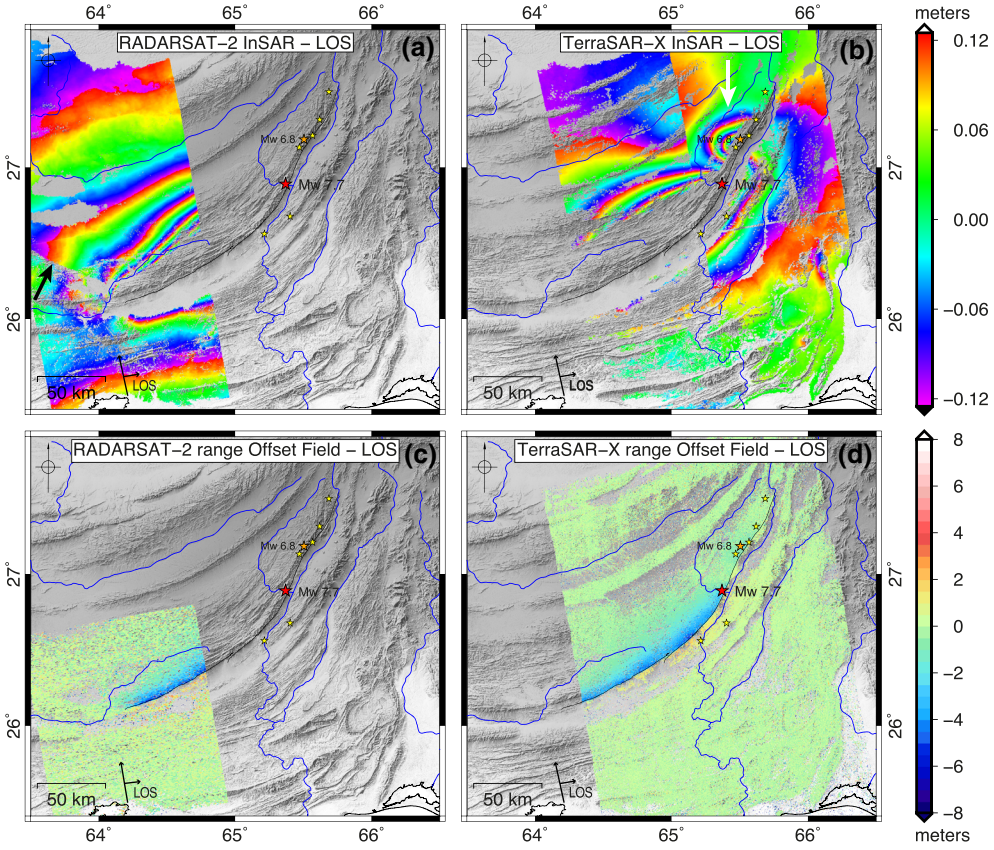


**Figure 3.** Interferograms (a and b) and radar range correlation (c and d) of RADARSAT 2 stripmap (a and c) and TerraSAR-X ScanSAR (b and d) radar scenes for the Balochistan earthquake. Each interferogram has been rewrapped to 24 cm of line-of-sight (LOS) displacement color cycle. Amplitude of displacement in radar correlation is positive when away from the satellite. Black arrow points a large-scale unwrapping error in RADARSAT 2 data, caused by an atmospheric front disrupting the fringe continuity. White arrow points the isolated deformation lobe visible in the NW block TerraSAR interferograms. Fault trace from Vallage et al. (2016), epicenter from Barnhart et al. (2014), aftershock epicenters from USGS.

35 km from the fault in the northwest block. These data also bring to light two lobes of deformation in the northwest block that spread on each side of the epicenter (Figure 3b). Such distribution of deformation is however not seen in the southeast block, where only one lobe of deformation is measured. Note also the existence of an unwrapping error, presumably due to a strong atmospheric front that we were unable to correct in the southern tile of RADARSAT-2 data (black arrow in Figure 3a).

In addition to interferometric measurements, we calculated range offsets of the radar images (Figures 3c and 3d). Correlating the pixels of two single look complex (SLC) SAR amplitude images provides coseismic measurements of the displacement in the LOS, as interferometric measurements, and along the azimuth direction (Elliott et al., 2007; Gold et al., 2015; Michel & Avouac, 1999; Roth et al., 2002). Due to limited azimuth resolution and to redundancy with optical image correlation, the azimuth component of SAR pixel offset correlation is not exploited further in the following. Correlation and topographic and orbital corrections were computed using ROI_PAC software (Rosen et al., 2004), resulting in displacement fields with a 115-m pixel size. While being noisier than InSAR data, offset field data are less affected by changes in the soil properties occurring around the fault and provide useful information near the fault trace, where no InSAR data are available.

In Figures 3c and 3d, negative displacements indicate ground moving toward the satellite while positive values show movements away from the satellite. Decorrelation is observed in both data sets, especially in places where the presence of basins degrades the radar signal. As for optical data (Figure 2), maximum displacements are measured in the middle and southern parts of the rupture, with up to 5 m in the LOS. The

displacement field is also asymmetric across the fault, with more displacements in the northwest block. Finally, by using radar range correlation, we coarsely measure LOS displacements in the medium (2–10 km away from the fault) and near fields (less than 2 km away from the fault). After taking into account the contribution of horizontal displacement projected in the LOS (derived from SPOT and Landsat data), such measurements confirm the occurrence of vertical motion for this earthquake.

### 2.3. Aftershocks and Post-Seismic Deformation

The data sets we use in this study all include early post-seismic deformation (afterslip) and up to several months of post-seismic deformation that we cannot separate from coseismic deformation. Several aftershocks (Figure 1) also occurred during the time span between the mainshock and the first post-quake acquisition, making it difficult to isolate their signal from the coseismic deformation. Since most of these aftershocks took place around the northern termination of the main rupture (Figure 1), RADARSAT-2 data are too far away from these aftershocks to measure any related ground deformation.

Landsat 8 acquisitions however do not bracket the most energetic Mw 6.8 aftershock of the sequence (28 September 2013, Mw 6.8, 27.183°N 65.505°E, GEOSCOPE centroid depth: 14.8 km, see Table S5 for seismological agencies data) while all other data sets include this event. Scaling laws from Wells and Coppersmith's (1994) study suggest a slip of ~2 m for a Mw 6.8 strike-slip earthquake. Given the precision of our measurements, this aftershock should be seen, its signal being larger than the order of the magnitude of the noise in the data (Landsat 8, SPOT 5 and SAR data). To estimate the impact of the Mw 6.8 aftershock in the optical measurements, we thus consider the difference between Landsat 8 and SPOT 5 data sets that both measure the same components of deformation. We find no significant shifts compared to areas where this aftershock has no influence (Figure S2), suggesting the aftershock occurred at depth and therefore is not associated with slip at the surface.

Furthermore, TerraSAR-X interferograms show two lobes (Figure 3b). The main lobe shows deformation on both sides of the fault and dwells from the epicenter area to the rupture southern termination. A smaller deformation lobe is centered on 27.1°N 65.5°E in the hanging wall (NW block), shown by the white arrow in Figure 3b. This deformation is not visible in the footwall and appears to be disconnected from the main lobe of deformation. We interpret this signal to be partly related to the Mw 6.8 aftershock: An aftershock taking place on the same fault plane and lacking a surface rupture would not be seen in the optical correlations but would be visible in the medium field of interferograms. Such an earthquake would explain our measurements and would be consistent with previous work from Zinke et al. (2014) who come to the same conclusion based on the comparison of different acquisitions of SPOT 5 and Landsat 8.

## 3. Surface Displacement Analysis

### 3.1. 3-D Surface Displacement Field

Maps of ground displacements in three different projections allow us to retrieve the NS, EW, and vertical components of the surface displacement (Fialko et al., 2001; Grandin et al., 2009; Wright et al., 2004). Here we have up to four different projections. We solve for the 3-D displacement (in the least squares sense) for pixels with displacement values for at least two independent horizontal vectors (optical data) and one sub-vertical vector (SAR data). This results in the complete 3-D surface displacement field of the Balochistan earthquake. The least squares solution attempts to minimize the norm of $b - A*x$ for each point, where $b$ is the available geodetic data, $A$ is the unit vector associated to the geometry of acquisition, and $x$ is the desired displacement in 3-D. For each point, we determine the 3-D solution that, when projected in the direction of each member of our database, satisfies the values of this data set. In terms of components, Landsat 8 and SPOT 5 data are redundant, as well as InSAR and radar correlation data. Despite different levels of noise, the different footprint of each data set allows us to have three independent components everywhere to solve for the three equations of the 3-D solution. The relative residual norm of this solution is presented in Figure S3. Profiles comparing the optical and radar original data and this 3-D solution are available in Figures S4 and S5, along with the projection of the 3-D solution in lines of sight (Figure S6).

The sharp break of surface displacement across the fault is visible (Figure 4), consistent with coseismic surface rupture. Both components show the same asymmetry across the fault we could see in the correlation data (Figures 2, 3c, and 3d), indicating a NW dipping fault. Furthermore, the displacement is concentrated

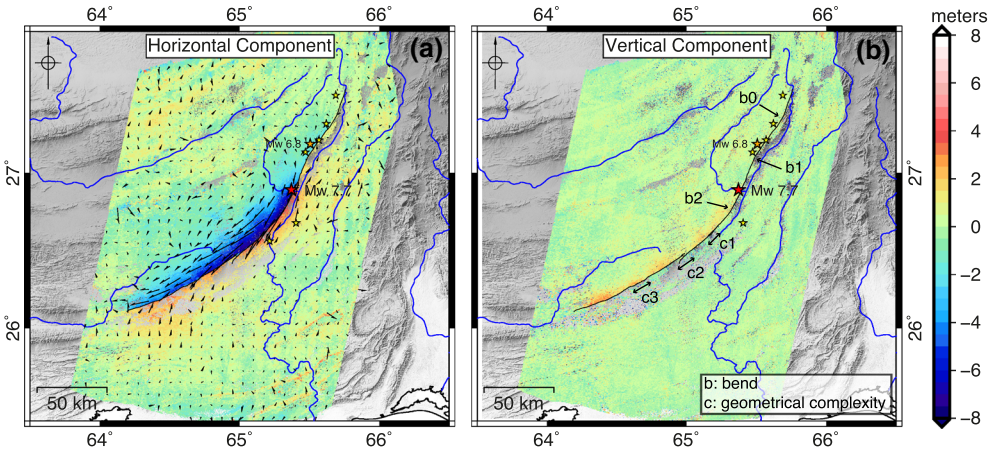


**Figure 4.** 3-D solution for surface deformation obtained from joint analysis of InSAR, radar correlation and optical correlation: horizontal (a: positive for northeastward motion) and vertical (b: positive for upward motion) displacement fields. Fault trace from Vallage et al. (2016), complexities and bends from Vallage et al. (2015), epicenter from Barnhart et al. (2014), aftershock epicenters from USGS.

near the fault, spreading over a distance of 15 to 30 km off the fault trace. This suggests slip mainly occurred at shallow depth. Maximum horizontal displacements are found in the middle and southern parts of the rupture, with up to 8 m (Figure 4a). The horizontal solution we find is fully consistent with already published horizontal data (Avouac et al., 2014; Barnhart et al., 2015; Gold et al., 2015; Vallage et al., 2015; Zinke et al., 2014). We also measure up to 3 m of vertical motion across the fault (Figure 4b), showing evidence for reverse slip associated to this earthquake, as showed by Barnhart et al. (2019). This motion induces an uplift of the NW block with respect to the SE block, consistent with a NW dipping fault with a thrust component.

### 3.2. Slip on the Fault and Dip Estimation Along Strike

In order to get a first order insight of the kinematics and geometry of the Balochistan earthquake, we analyze the relative displacement across the fault, along the rupture. We compute a total of 90 cross sections using the vertical component of our 3-D solution (Figure 4b) and the horizontal components of SPOT 5 data (Figures 2c and 2d, which is more precise than our 3-D solution due to the combination with Landsat 8 data). For each cross-section we model the displacement on each side of the fault as straight lines and measure the offset across the fault. Uncertainty is estimated for each component of the slip by considering the fit of this model with respect to the data (envelopes in Figure 5a, quadratic difference between observations and model. We consider the data over a distance of up to 12 km from the fault trace to capture mid-field deformation and limit noise perturbations. We also mask the first 500 m on each side of the fault to avoid previously highlighted complex near-fault deformation patterns (Barnhart et al., 2015; Gold et al., 2015; Vallage et al., 2015; Zinke et al., 2014). Horizontal offsets are then rotated from east-west and north-south to fault-parallel and fault-normal components by considering a local azimuth for each profile. No transformation is applied to the vertical component. Retrieval of each profile position along the fault finally allows us to construct the slip curves (Figure 5a), with a mean uncertainty of 0.23 m for the fault parallel, 0.24 m for the fault normal, and 1.53 m for the vertical components.

The slip curves show variations in the horizontal components of the surface slip over a few kilometers (Figure 5a). We checked that this variability is not a consequence of along-strike variations in the definition of the cross-section orientations. The vertical offset (red curve in Figure 5a) along the fault is subjected to noise, which is probably due to the presence of basins south of the fault, where the radar data have a poor coherence. Despite this limited accuracy, we can compute a mean vertical offset of 1.3 m and a maximum of 4.9 m, which is consistent with the average of 1.9 m and maximum of 5.6 m proposed by Zhou et al. in 2015 on a 1-m resolution post-earthquake elevation model. Despite some discrepancies, our results are also consistent with values proposed by Zhou et al. (2018) (Figure S7a) and by Barnhart et al. (2019) (average of 2 m, Figure S7b). The fault-normal motion (green curve in Figure 5a) is

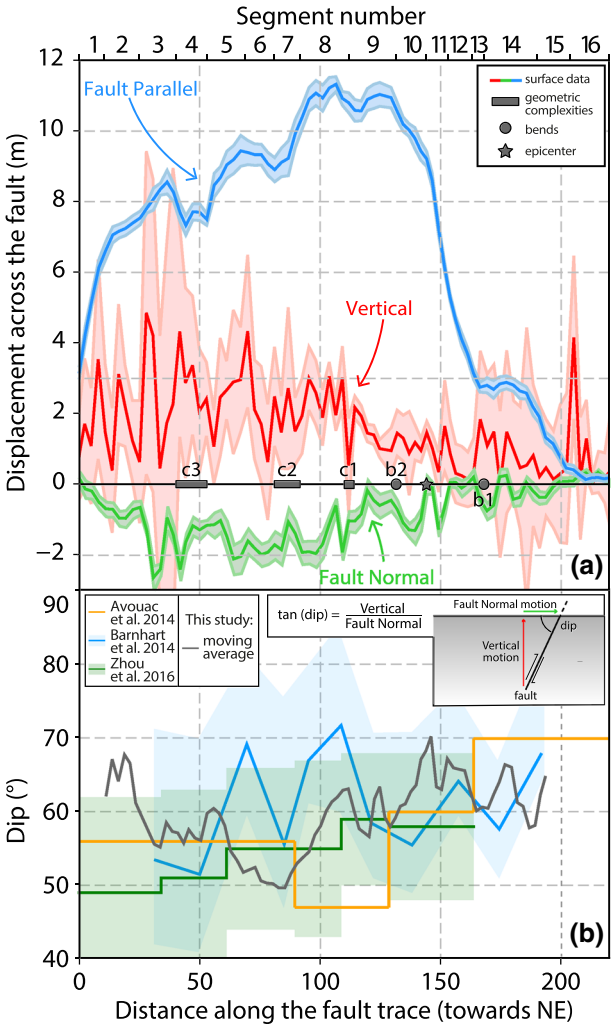


**Figure 5.** (a) Along-strike distribution of surface slip. Fault-parallel and fault-normal components are respectively in blue and green and are derived from SPOT correlation data. The fault-parallel motion is positive since the relative motion is left-lateral; the fault-normal motion is negative since the relative motion is convergent. Vertical component is in red and is derived from the 3D solution visible in Figure 4b, positive values stand for an uplift of the northern block. Gray polygons and star stand for geometric complexities and epicenter, respectively (see location in Figure 4b). (b) Dip estimations along the strike of the fault estimated from the ratio of vertical over fault-normal displacements (this study) are in gray. Values found by Avouac et al. in 2014 and Zhou et al. in 2016 are respectively in orange and green. Complexities from Vallage et al. (2015) (see Figure 4 for location), epicenter from Barnhart et al. (2014). Segment numbers correspond to the fault trace discretization that is detailed in section 4.1.

negative since the relative motion is convergent and has a mean of 0.7 m and a maximum of 2.6 m. The mean of the fault-parallel motion (blue curve in Figure 5a) is 6.1 m, and its maximum is 11.3 m. Values for both horizontal components are in good agreement with previous studies, based on optical cross-correlation of Landsat 8 (Avouac et al., 2014; Barnhart et al., 2014), WorldView (Barnhart et al., 2015), and SPOT 5 images (Vallage et al., 2015). Finally, the slip curves confirm the predominance of left-lateral strike slip for this earthquake but also show substantial thrust and vertical components.

The ratio between vertical displacement and fault-normal displacement allows us to estimate the fault dip at the surface (Figure 5b). We thus compute the dip for each profile and represent its variations along the fault trace, bearing in mind that these shallow dip variations may not necessarily be representative of the deeper structure. Figure 5b shows that dip angles are significantly spread; we obtain an average dip of 66 degrees ± 13, consistent with studies from Avouac et al. (2014), Jolivet et al. (2014), and Zhou et al. (2015) (50–70°N). We compute a moving average using a window size of 5 points (~10 km, Figure 5b). Dip values still show variations that might be a clue for a variable dip along the fault: At a first order, one can notice a local shallowing of the fault dip with 57° from 75 to 110 km, that is, at the center of the rupture, compared to North (68° at 0–40 km) and South (70° at 160–215 km) extremities of the rupture. We hypothesize that the shallowing of the dip angle in the junction between the Chaman Fault System and the interior of the Makran accretionary wedge might be the only way to connect these two sub-vertical terminations in one single fault.

Retrieving the 3-D displacement field of the Balochistan earthquake finally allows to characterize the vertical displacement field (Figures 4b and 5a). The vertical component is particularly large at specific locations, as near the first and third geometrical complexities (c1 and c3 from the Vallage et al., 2015, see location in Figure 4b) and also in the southern termination area, while the horizontal component has a smoother distribution all over the fault. One can especially note that, going southward, the vertical and fault-normal components are doubling from complexity c1 (Figure 5a), which is where the fault dip is starting to decrease (Figure 5b) and the fault orientation to change to link with the Makran accretionary prism (Figure 5a). Furthermore, the location of complexities matches well with local lower values of strike-slip motion across the fault. These along-strike variations could be due to the fault structure complexity and lateral segmentation. As a matter of fact, complexities, such as bends or push-up, are indeed known to disrupt the earthquake behavior and prevent the rupture from propagating fully (Aki, 1979; Choi et al., 2018; Klinger et al., 2006). Understanding the patchy pattern of the vertical displacement field and its variations along the fault requires a better knowledge on the fault geometry and the slip at depth that we try to constrain in the following parts.

## 4. Non-Linear Inversion of Fault Geometry

Modeling the position, length, strike, width, dip, slip, and rake for several dislocations is numerically challenging. Therefore, we adopt a three-step approach. We first determine a set of fault segments to describe the Hoshab fault (number, position, length, and orientation). We then non-linearly invert the geometry for each segment (dip and down-dip dimension), and we finally linearly invert for the slip distribution (slip and rake).

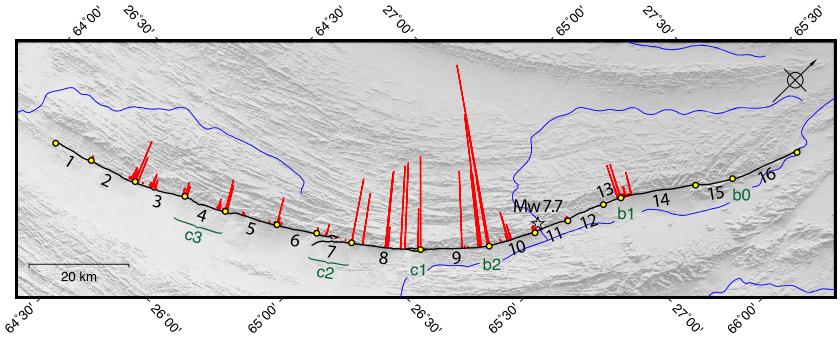


**Figure 6.** Histogram (red bars) along the fault, showing the number of occurrences when a point of the fault trace is selected as an inter-segment in our automatic discretization procedure, assuming the fault consists of 16 segments. Numbering corresponds to our final discretization, and yellow dots represent the final picked inter-segments. Fault trace from Vallage et al. (2016) in black, complexities c1 (relay zone), c2 (push-up), c3 (paired-bend) and bends b0 to b2 from Vallage et al. (2015) in green, epicenter (gray star) from Barnhart et al. (2014).

### 4.1. Optimal Number, Location, and Orientation of Fault Segments

First, we model the surface rupture as a continuous set of linear segments defined by their location, length, and orientation (strike). The trace is however complex. Vallage et al. showed in 2015 that slip partitioning occurred, with fault-parallel cracks localized in the hanging wall while the fault-normal features concentrate at the front. Major geometrical complexities also punctuate the rupture with, from north to south, three bends (b0, b1, and b2), two relay zones (c1 and push-up c2) and one paired-bend (c3) (Vallage et al., 2015) (Figures 4 and 6). This level of complexity requires us to consider a rupture zone rather than one unique rupture trace. To simplify this problem, we only digitize the envelope of the rupture zone, with the strike-slip segments inboard of the Makran wedge on one hand and the more external thrusts on the other hand. We also generate a hand-picked general trend that stands for the mean path of the rupture. Furthermore, we let the fault segments extend 25 km further north from the northern end, where geodetic data show some coseismic displacements north of the mapped surface rupture and where aftershock activity has been registered. Each mapping covers the whole ~220 km rupture and has a resolution of 1 point every ~100 m.

We use this extensive fault trace map and process it using the automatic procedure developed by Klinger (2010), which is based on the "L1 trend filtering" method (Kim et al., 2009). This procedure tests different sets of segments to approximate the fault trace. We explored 13,500 unique segment distributions, each one being defined by a number of segments (5 to 90) and a given spatial distribution of the segments. With the help of a trade-off curve, we find that 16 fault segments are the best compromise between number of segments and misfit (quadratic difference between observations and model). In the following, we thus concentrate only on inter-segment distributions with 16 segments. Figure 6 shows a histogram along the fault trace that represents the number of times when a point of the fault trace is selected as an inter-segment (i.e., a point that separates two segments) among models with 16 segments. A few points are frequently selected as inter-segments and seem spatially linked with the geometrical complexities: The bends b0, b1, and b2 and the relay zone c1 indeed form inter-segments while the double-bend c3 consists in one segment itself. We finally pick 17 inter-segments from the redundant points (yellow dots in Figure 6), resulting in 16 segments. Comparison to slip curves (Figure 5a) shows slip variations match well with our segment distribution. Segment 4 matches both the complexity c3 (Figure 6) and a lower fault-parallel motion (Figure 5a) while complexity c1 is consistent with the transition from segment 7 to 8 (Figure 6) and a local lower fault-parallel value (Figure 5a).

### 4.2. Fault Geometry and Slip Distribution on Planar Segments

#### 4.2.1. Main Approach

We now fix the horizontal position, strike, and length of the fault segments using the previous results. Each segment is considered as a single planar dislocation with uniform slip and no opening, and we impose that the segments go up to the surface. The dip and width (down-dip dimension) are now the parameters we want to estimate, along with the slip and rake. Because the fault geometry is not specified a priori, the problem is non-linear. We use a Quasi-Newton inversion algorithm (Tarantola & Valette, 1982), and Okada's equations

for the forward calculation (relationship of rectangular dislocations embedded in a homogeneous half space to surface displacements; Okada, 1992). In the following, we do not use the 3-D solution from Figure 4; instead, we always consider the original geodetic data from Figures 2–3.

To initialize the inversion, we first invert the geometry of each fault segment separately, considering 100-km long data profiles that go through the middle of each segment. We provide no constraints on the length of the segments, and we use the dip estimates from Figure 5b as starting values. This produces a first rough estimate for the dip and width of each fault segment that we subsequently use as an input model to invert for the 16 segments together, using the full data set. By using the whole data set, we expect to constrain the deeper structure of the fault.

To reduce the computational task, we subsample the data using a spatially variable sampling (Jónsson et al., 2002; Lohman & Simons, 2005; Simons et al., 2002) that gradually decreases the density of each data set with the distance from the fault (Grandin et al., 2009). However, such a simple model (16 segments) cannot reflect the rupture complexity. Therefore, we cannot expect a good fit to the data in the direct vicinity of the fault and mask the data within 2 km of the fault. We finally decrease the number of data points from 23.7 million to 4,453. Moreover, we use all available observations (Landsat 8, SPOT 5, RADARSAR-2, and TerraSAR-X, Figures 2 and 3), and we treat the data sets as independent and equally weighted for this modeling step.

As discussed before (Section 2), the 28 September 2013 Mw 6.8 aftershock is not visible in the optical data whereas it is marked in the interferograms by a lobe of interferometric fringes northwest of segments 14 and 15 (white arrow, Figure 3b), implying the aftershock was not superficial. This hypothesis is consistent with depths provided by seismological agencies (12 to 15 km, see Table S5). Furthermore, the location of the lobe of fringes suggests the aftershock also took place on the Hoshab fault. Hence, our approach uses an additional two-fault slip model to take into account this aftershock. We divide segments 14 and 15 in two sub-segments along depth that form a continuous plane but are allowed to have different slip and rake values. Shallow sub-segments are supposed to reflect the mainshock and the deep ones, the aftershock. The depth of the sub-planes demarcation has been adjusted by trial and error. At the end, we expect the mainshock to explain the optical data and a part of the interferograms and the aftershock to explain the rest of InSAR signal.

To model the MW 6.8 aftershock, we isolate the deformation lobe visible in the TerraSAR-X interferogram (white arrow in Figure 3b) and invert for the slip and rake on the patches at depth of segments 14 and 15. Explaining such a deformation pattern requires a seismic moment of 3.53 $10^{19}$ Nm, which is 1.5 to 2 times larger than the seismic moments provided by seismological agencies for the Mw 6.8 aftershock (1.8 to 2.3 $10^{19}$ Nm from USGS, Global CMT, and GEOSCOPE, see Table S5). This larger seismic moment suggests that the deformation lobe we see in the interferogram in Figure 3b is a consequence of both the main shock and the aftershock. We therefore impose a 2.0 $10^{19}$ Nm seismic moment for the aftershock to be consistent with seismology. By doing so, we should limit the incorporation of deformation due to the main shock in the aftershock model. We then correct TerraSAR-X data sets from the contribution of the aftershock by removing the synthetic model from the data. Despite low horizontal values (maximum of 30 cm), we decided to correct SPOT 5 data as well, for the sake of processing consistency. We use these corrected data to invert for the dip, width, slip, and rake of the 16 segments, for the main shock. We ensured the consistency of the dip of the shallow (mainshock) and the deep (Mw 6.8 aftershock) patches of segments 14 and 15, by going back and forth between the models of both shocks until having a good convergence.

#### 4.2.2. Results

Seismic moment, average rakes, dip, and depth for the Mw 6.8 aftershock are consistent with focal mechanisms provided by USGS, Global CMT, and GEOSCOPE (Figure 7h and Table S5). The depth and rake we found are also consistent with our hypothesis of an aftershock at depth, also supported by Zinke et al. study in 2014. Finally, when using the scaling laws from Wells and Coppersmith (1994), we find a rupture width of 16.5 km for a magnitude of 6.8 which is also consistent with our results. In Figures 7a–7g, we compare the contribution of the aftershock and the main shock which shows that the sum of the two finally explains the data.

Due to the small intensity of deformation in the vicinity of segments 15 and 16, dip estimations were unstable. We therefore fixed a dip of 89° for these two segments, consistent with the linkage of the

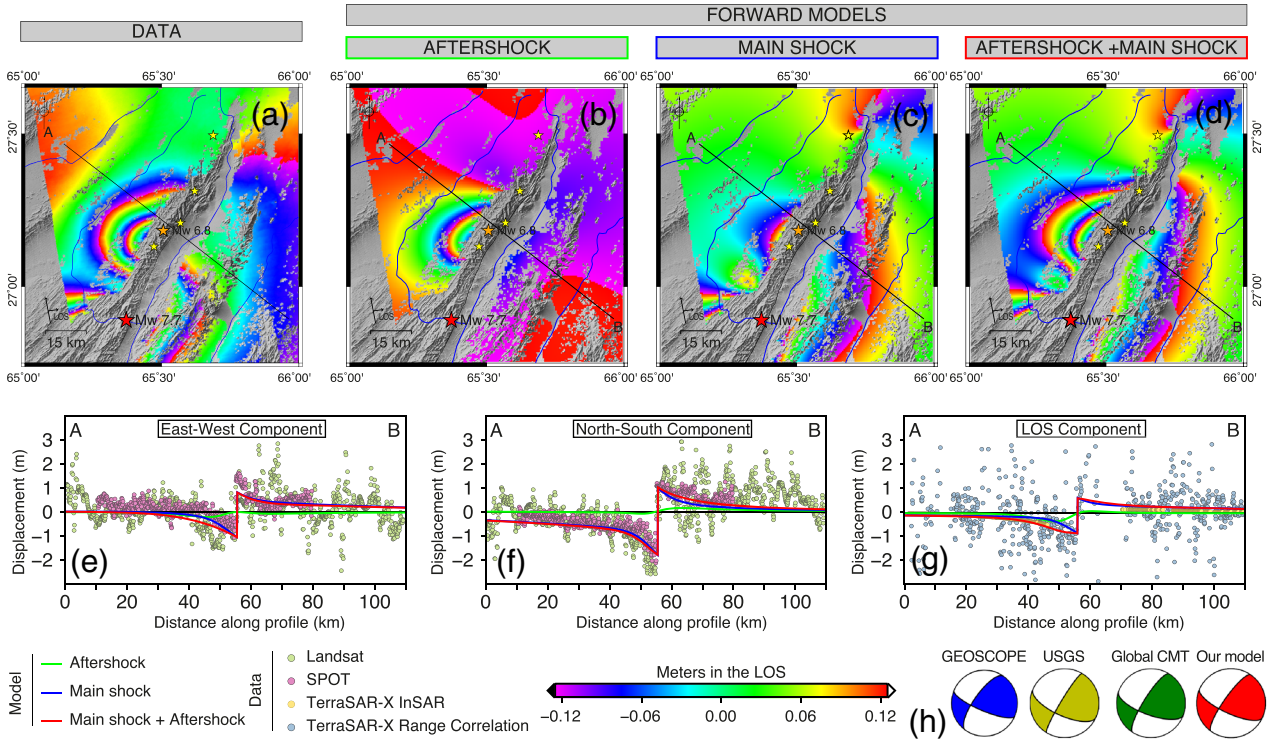


**Figure 7.** Results from the non-linear inversion. Maps (c and d): Synthetics projected in the TerraSAR-X line of sight in the vicinity of the main aftershock, showing the contribution of the main aftershock (28 September 2013 Mw 6.8 (b)), the main shock (c) and the final model (d), to compare with the data (a). Each color cycle represents 24 cm of LOS displacement. Profiles (e–g): Profile A-B showing the same contributions as above (solid lines) along with the data (dots) for three components (EW (e), NS (f), TerraSAR-X LOS (g)). Focal mechanisms (h): Main Mw 6.8 aftershock from three different agencies and our model (red). Fault trace from Vallage et al. (2016), epicenter from Barnhart et al. (2014), aftershock epicenters from USGS, focal mechanisms from USGS, Geoscope and Global CMT.

Hoshab fault on the Chaman fault system. Overall, results give a mean dip of 67° (to the northwest) that varies between 50 and 89° (Figure 8d). This is consistent with previous studies (Avouac et al., 2014; Barnhart et al., 2014; Jolivet et al., 2014). Dip values deduced from the surface data analysis (section 3) and from the non-linear inversion are in good agreement.

The along-strike distribution of dip angles (violet curve in Figure 8d) shows a shallowing of the fault dip angle in its central part, framed by two sub-vertical sections. North of the epicenter, the fault shows steeper dip values (70 + °) consistent with the linkage with the vertical structures of the Chaman strike-slip fault system. In its southern termination, the fault is also steeper, consistent with a steepening of the structures toward the interior of the wedge (Malavieille, 1984). The central shallowing of the fault dip angle may be the structural expression of the transition between two vertical structures that are perpendicularly oriented. Concerning the depth of fault segments, the non-linear inversion returns a bottom depth with a mean of 8.8 km with no significant variations along strike (orange curve in Figure 8e). Such results support the previous models that highlighted a predominantly shallow rupture (Avouac et al., 2014; Barnhart et al., 2014; Jolivet et al., 2014) and suggest that the earthquake did stop at depth near the décollement level, inferred at 12 km depth (Ellouz-Zimmermann et al., 2007).

The non-linear inversion also gives an overview of the fault kinematics (Figures 8a and 8b). North of the epicenter, coseismic slip is rapidly decaying. South of the epicenter, results suggest a maximum slip of 10.8 m. Strike slip goes up to 10.6 m while dip slip maximum is 3.2 m. Starting from the epicenter, strike slip increases rapidly to its maximum value (segment 8) and decays southwestward while the fault is increasingly oblique to the direction of main stress. This change in orientation also leads to the southwestward strengthening of the dip slip component, with a maximum near the southwest termination (segment 2).

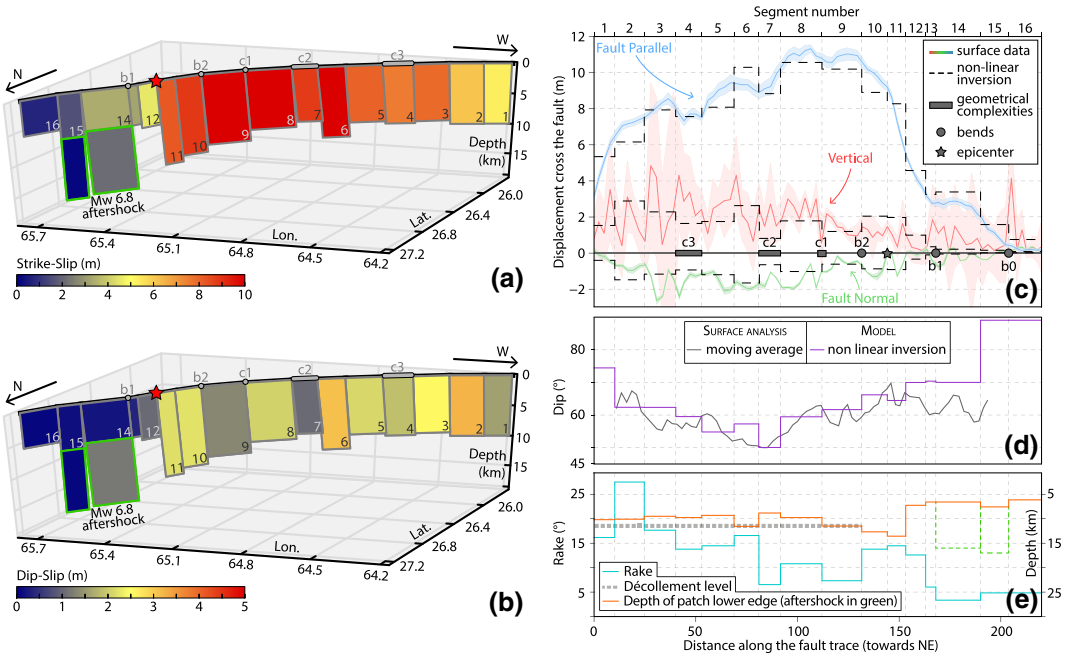


**Figure 8.** Results from the non-linear inversion with slip distribution at depth (a and b) and along-strike distribution of fault parameters estimates (c and e). (a): Slip distribution for the strike-slip component. (b): Slip distribution for the dip slip component. For both slip distributions, segments 1 to 16 are associated to the main shock (Mw 7.7) while segments with a green frame are related to the 28 September 2013 Mw 6.8 aftershock. (c and e): Along-strike distribution of fault parameters. (c): Solid lines represent the surface slip curves deduced from surface displacement (Figure 5a), dashed lines represent the same parameters for each fault segment from the inversion. (d): Gray line is the dip from Figure 5b, violet line stands for the dip of each segment estimated by the inversion. (e): Cyan and orange curves respectively represent the rake and depth of each segment from the inversion. Complexities from Vallage et al. (2015), epicenter from Barnhart et al. (2014), décollement level from Ellouz-Zimmermann et al. (2007).

Predictions are also in good agreement with the slip curves despite some discrepancies that are presumably due to the coarseness of this first modeling step (Figure 8c). The slip curves from the Vallage et al. (2015) study were based on near-field (<1 km) measurement in SPOT 5 data and informed on very shallow slip on the fault. The slip curves we obtained in Section 3 are smoother because they are based on mid-field deformation (2–12 km off the fault) and integrate information on processes taking place at greater depth. Here, the inversion is assisted by the elastic model and reflects integrated slip on the fault. Slip predictions on the fault show a fairly simple distribution along depth. The similarity of all slip curves suggests that surface slip is consistent with slip at depth, meaning that for the Balochistan earthquake, knowledge on the surface slip is enough to estimate the slip at depth.

Finally, as expected, synthetics reproduce the gradient of deformation to a first order (Figures 9 and S8–21). To explain more details and improve the fit to the data, we fix the geometry and now proceed to a linear inversion, using the geometry.

## 5. Distributed Slip Model

### 5.1. Main Approach

To determine finer details of the coseismic slip distribution, we now discretize the fault segments into ~3 km × 2 km fault patches. We do not use the depth values found in section 4 and choose to extend the depth of all segments to 18 km. The segments dip angle is fixed according to our previous results (Figure 8d). In this last modeling step, we invert the data for variable slip and rake only. The problem is linear and is solved using the Python Classic Slip Inversion library (Jolivet et al., 2014). We consider an Okada solution (Okada, 1992) for the Green's functions, and we use non-negative least squares (Lawson & Hanson, 1974), only allowing for left-lateral strike slip and dip slip.

The data we use are corrected from the Mw 6.8 aftershock. We proceed to a less stringent decimation to allow for more details, while still masking the data within 2 km of the fault. We finally obtain 25,172 data points

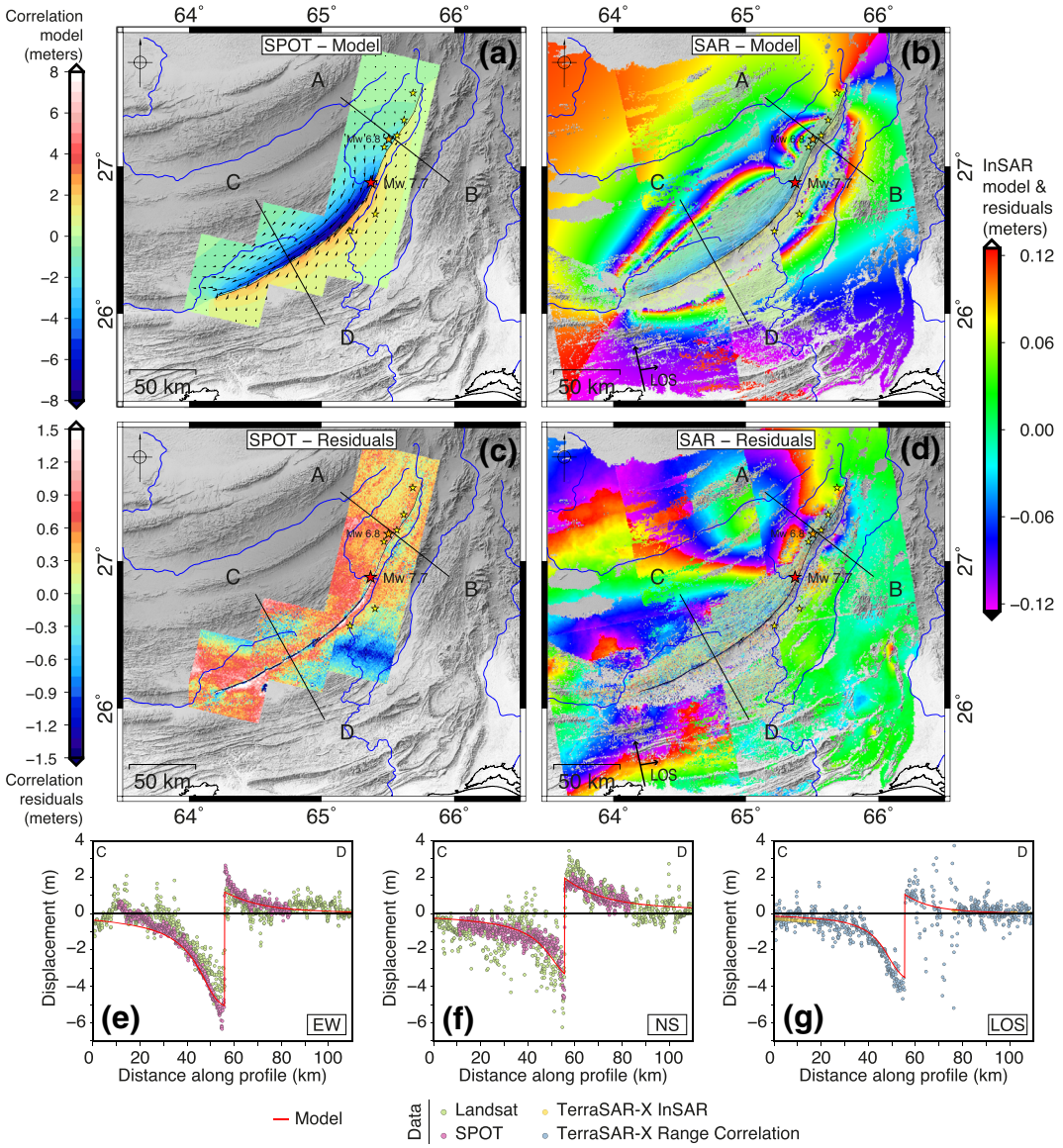


**Figure 9.** Results from the non-linear inversion. (a and b): Synthetics showing the predicted coseismic horizontal component ((a) positive for northeastward motion) and the projection of coseismic displacements in the TerraSAR-X LOS ((b) each color cycle represents 24 cm of LOS displacement). (c and d): Residuals. (e and g): Profile C-D showing the model predictions (solid lines) along with the data (dots) for three components (EW (e), NS (f), TerraSAR-X LOS (g)). Fault trace from Vallage et al. (2016), epicenter from Barnhart et al. (2014), aftershock epicenters from USGS, focal mechanisms from USGS, Geoscope and Global CMT.

(23.7 million in the raw data, 4,453 for the non-linear inversion). As for the non-linear inversion, we still treat all observations as independent and use all the data sets (Landsat 8, SPOT 5, RADARSAT 2, and TerraSAR-X). To avoid strong variations in the fault slip between neighboring patches, we set up a Laplacian smoothing scheme (Menke, 1989). No smoothing is carried out between fault segments and the optimal smoothness factor is chosen with the help of a trade-off curve. We also attempt to reduce the effects of orbit errors by solving for the best-fitting plane in each data set as a part of the inversion.

Besides, we proceed to a resolution analysis to test the capability of our model to provide information on the slip amplitude and location (Radiguet et al., 2011). For a given patch, the resolution (Figure S22a) indicates how much the slip of this patch is actually mapped to this patch by the inversion. As expected, the resolution decreases rapidly at depth, especially below 4 km, consistently with Jolivet et al. (2014). Nevertheless, the

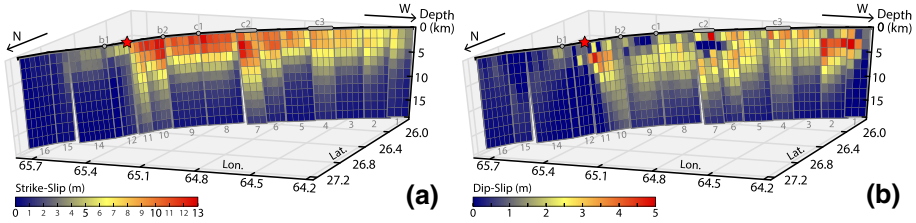


**Figure 10.** Results from the linear inversion. Slip distribution for the strike-slip (a) and dip slip (b) components. Complexities from Vallage et al. (2015), epicenter from Barnhart et al. (2014).

restitution (Figure S22b) shows most areas where coseismic slip is found in the model have a good restitution index (i.e., higher than 0.8). In other areas, the inversion is however unable to allocate slip.

### 5.2. Results

As expected, results show a dominant strike-slip motion forming a continuous slip patch concentrated south of the epicenter (Figure 10a). The strike-slip component peaks at 12.8 m 20 km to the south of the epicenter (segment 10) and decreases slowly going southward, before terminating abruptly. Most of the slip is confined between the surface and 8 km depth. While the slip continuously reaches the surface, its lower limit is irregular along strike with depths ranging from 8 to 14 km. Starting from the epicenter and going southward, we observe a general trend for this lower edge to get shallower. This general trend is however irregular due to a deepening of the slip at few places, as noticed between segments 8 and 7 and between segments 5 and 4. We interpret this behavior as reflecting a weakening of the slip when the rupture propagates through the areas with a change in the dip (Figure 8d), followed by a regain in the amplitude and extension on the next fault segment.

The dip slip component is more heterogeneously distributed, with several patches of moderate amplitude separated by smaller slip values (Figure 10b). Very little slip is found north of the epicenter. As for the strike-slip component, reverse slip is mostly confined between 0 and 8 km depth and seems to get shallower going southward. Local minima in the lower edge of the patches occur at the same locations we highlighted for the strike-slip component. Some slip gaps are also found, as the one visible in segment 7, between 2 to 4 km depth, but we suspect these gaps to be numerical artifacts. Maximum amplitudes are found in segments 1, 2, and 11 with 5.3, 4.8, and 4.7 m, respectively.

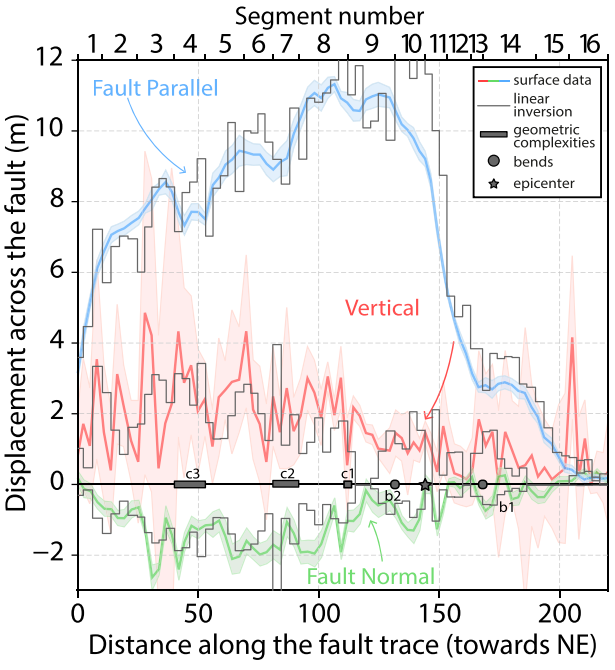


**Figure 11.** Slip along the strike of the fault. Surface data (Figure 3.2) are in color (blue for fault-parallel, green for fault-normal and red for vertical). Gray lines represent the slip on the shallowest patches, in the correspondent components. Complexities from Vallage et al. (2015), epicenter from Barnhart et al. (2014).

Our solution gives a seismic moment of 3.64 $10^{20}$ Nm (USGS: 4.42 $10^{20}$ Nm, GEOSCOPE: 6.41 $10^{20}$ Nm). The seismic moment released by the strike-slip component accounts for 3.15 times the moment associated with the dip slip component.

Near-surface slip values along the strike reproduce well the slip curves obtained from surface data analysis (Figure 11), except for segment 10 for which the inversion yields too high values. Difference between models and data (Figures 12, 13, and S8–21) also show that we explain most of the signal despite some discrepancies, especially in the near-field, that may be due to local inadequacies of the elastic model, the use of a simple geometry, the discretization of fault patches, and/or data processing errors.

A long wavelength residual also exist in the northern part of the TerraSAR-X data at 65°N 27.5°E. Surprisingly, this signal is also visible in ascending Sentinel-1a interferograms that span from December 2014 (15 months after the earthquake) to December 2016 (Peterson et al., 2018), while our TerraSAR-X post-event scenes were acquired in December 2013 and July 2014. Such signal may be explained by either a local shallow source of deformation near 65°N–27.5°E or a deeply rooted

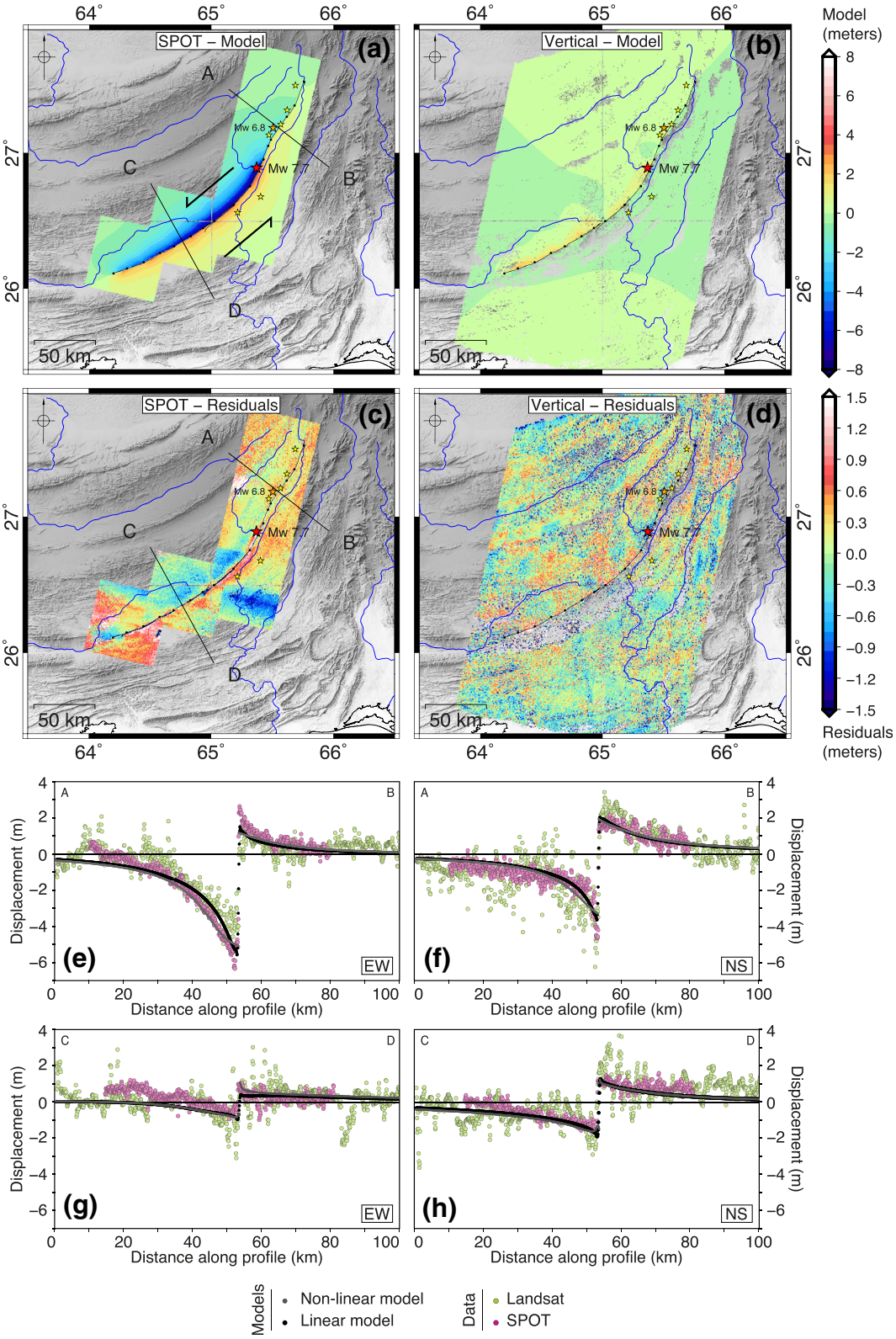


**Figure 12.** Results from the linear inversion. Top maps: Synthetics showing the predicted coseismic horizontal component (left: positive for northeastward motion) and predicted coseismic vertical component (right: positive for upward motion). Bottom maps: Corresponding residuals. Profiles: Profile C-D for EW (left) and NS (right) components. The gray dots represent the non-linear inversion, the black points stand for the linear inversion. Color dots (green and magenta) corresponds to the data. Fault trace from Vallage et al. (2016), epicenter from Barnhart et al. (2014), aftershock epicenters from USGS.

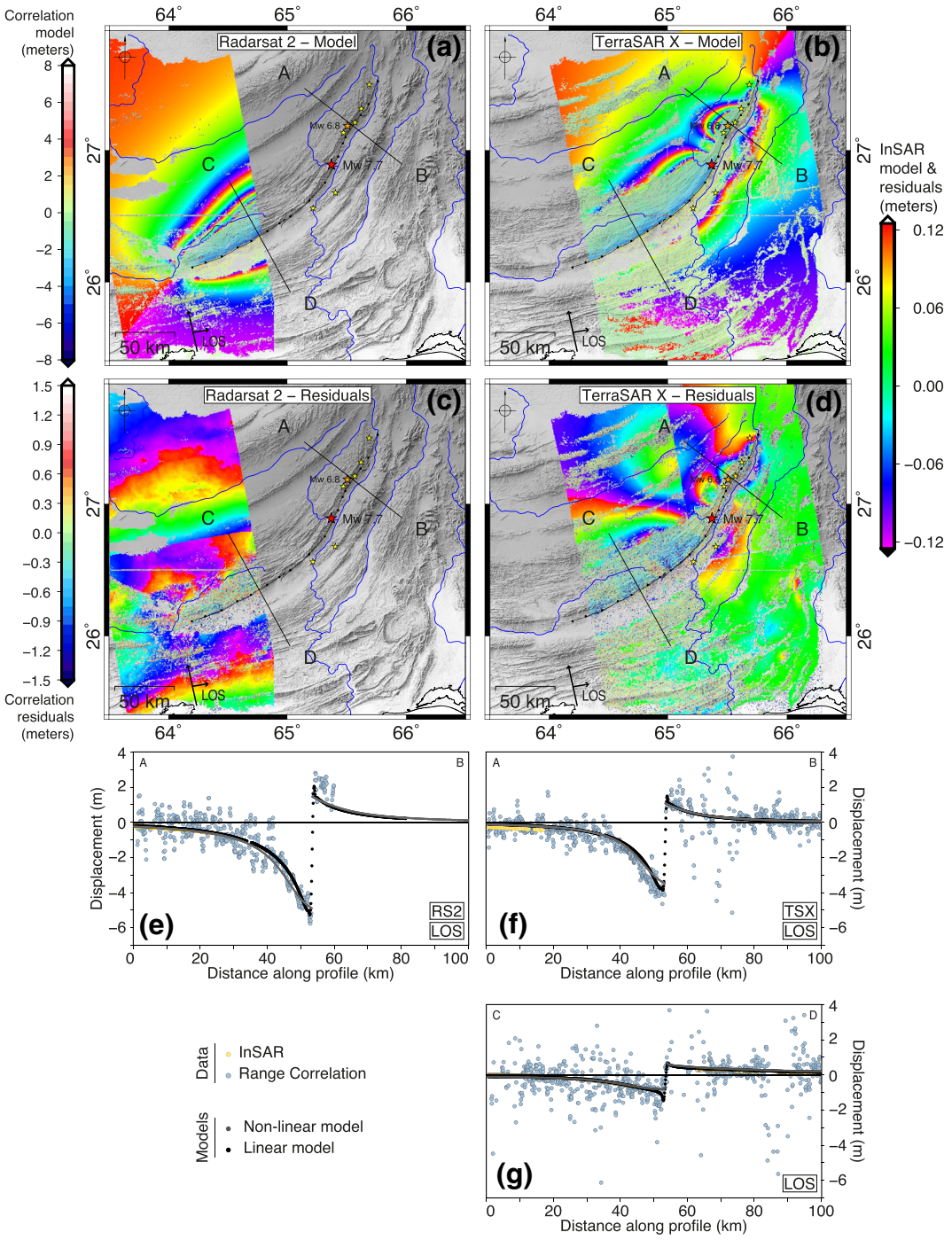


**Figure 13.** Results from the linear inversion. Top maps: Synthetics showing the predicted displacements in the RADARSAT-2 LOS (left) and in the TerraSAR-X LOS (right: each color cycle represents 24 cm of LOS displacement). Bottom maps: Corresponding residuals. Profiles: Profile C-D for RADARTSAT-2 (left) and TerraSAR-X (right) components. The gray dots represent the non-linear inversion, the black points stand for the linear inversion. Color dots (green and magenta) corresponds to the data. Fault trace from Vallage et al. (2016), epicenter from Barnhart et al. (2014), aftershock epicenters from USGS.

process in the vicinity of the Hoshab fault. Such sources would however have no interferences with our modeling.

Finally, we also proceeded to the same linear inversion but with the original data, that is, not corrected from the main Mw 6.8 aftershock model (Figure 7). Results are visible in Figure S23 for each component of the slip

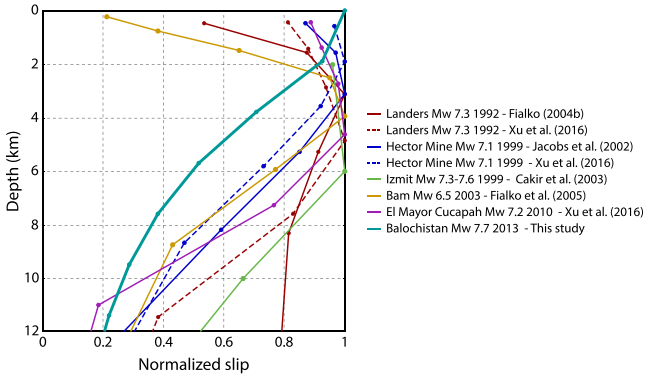


**Figure 14.** Normalized slip as a function of depth for several large strike-slip earthquakes. Each color represents one earthquake. See legend of figure for references.

and show that we are able to recover the synthetic slip that we attributed to the aftershock and that was removed from the data.

## 6. Discussion

### 6.1. Absence of Shallow Slip Deficit During the Balochistan Earthquake: A Feature of Strike-Slip Earthquakes Related to Magnitude and Tectonic Context?

For large strike-slip earthquakes, models of coseismic slip based on geodetic data alone commonly yield a discrepancy of slip between intermediate depths and the uppermost part of the crust, a phenomenon known as "shallow slip deficit" (hereafter SSD). This difference is characterized by a maximum release of seismic moment in the middle of the brittle layer (between 4 and 8 km depth) that decreases toward the surface (Figure 14) (Fialko et al., 2005).

The SSD raises questions on the integration of such discrepancy through the seismic cycle. Several physical mechanisms could accommodate part of the SSD such as shallow creep, post-seismic afterslip, or distributed inelastic failure (Fialko et al., 2005). Larger past and future earthquakes, or even smaller events, could also break the shallowest parts of faults and bring this discrepancy to zero through time (Simons et al., 2002). Alternative explanations involve the maturity of the fault zone, which is defined by the displacement accumulated over time by the fault, with more shallow slip deficit for immature faults (Dolan & Haravitch, 2014).

The capacity of geodetic models to correctly characterize this shallow slip deficit has strongly been questioned. Models may be unrealistic (elastic vs. inelastic deformation) and methodology deficiencies have been pointed out with modeling bias and data incompleteness. Classic elastic models indeed do not account for inelastic deformation (Fialko et al., 2005; Gombert et al., 2017; Kaneko & Fialko, 2011; Simons et al., 2002; Vallage et al., 2015; Xu et al., 2016) and for spatial variations of rock properties (Sudhaus & Jónsson, 2011), leading to biased estimations in the slip distribution. Inaccurate models of fault geometry (Ragon et al., 2018) and model smoothing have also been shown to play a role in shallow slip estimations. For example, more deficit is found for smoother models (Huang et al., 2017; Marchandon et al., 2018; Xu et al., 2016). In addition, using near-fault data such as high-resolution optical correlation has recently shown a decrease of shallow slip deficit from 15–60% to only 3–19% for three major strike-slip earthquakes: 1992 Mw 7.3 Landers, 1999 Mw 7.1 Hector Mine, and 2010 Mw 7.2 El Mayor–Cucapah (Xu et al., 2016) (see dashed lines in Figure 14). Likewise, incorporation of across-fault offsets in models yields a smaller shallow slip deficit (Marchandon et al., 2018). This suggests the SSD is overestimated when near-field data are missing. Finally, setting aside the effect of local topography by using half-space models may, in some cases, lead to an underestimation of coseismic shallow slip (Thompson & Meade, 2018). Recent studies thus showed that the modeling procedure itself may lead to overestimate shallow slip deficit but were however unable to bring this discrepancy to zero (Marchandon et al., 2018; Xu et al., 2016). This suggests a part of the measured shallow slip reflects reality and is not only imputable to modeling considerations.

Here, we modeled the coseismic slip using a complete geodetic data set in terms of both coverage and geometry of acquisition. The three-step modeling approach we adopted allows us to be confident in our conclusions, with robust assumptions on both the fault geometry and the kinematics of this event. Previous studies show no shallow slip deficit for the Balochistan earthquake (Jolivet et al., 2014; Vallage et al., 2015). Our model yields very consistent results with neither evidence of shallow slip deficit (Figure 15). Conversely, in our model, the coseismic slip almost constantly peaks at the surface all along the rupture.

Three segments are an exception to this shallow slip maximum: segments 1, 2, and 7 (Figure 15). The first two correspond to the southeast earthquake termination and show the strongest reverse component; such features may explain the ~11% shallow slip deficit we measure. On the other hand, segment 7 delineates complexity C2 (Figure 15). At this location, the fault shows a complex pattern with several strands (Vallage et al., 2015) that may propagate at least in the first kilometers of the crust. By coarsely modeling these strands with only one single fault, we oversimplify the fault geometry, possibly leading the model to

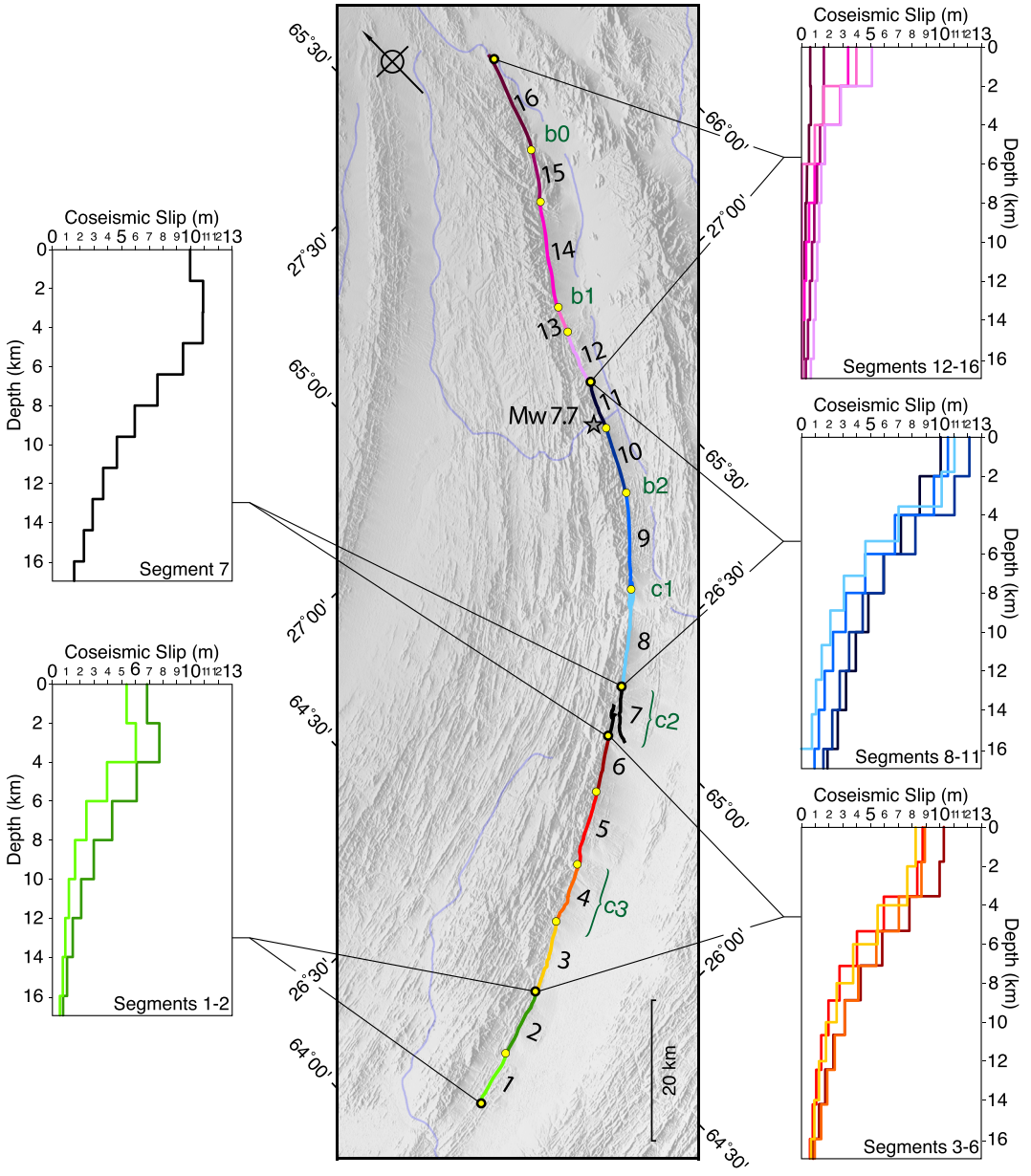


**Figure 15.** Mean slip as a function of depth for the 16 segments of the Hoshab fault. Complexities from Vallage et al. (2015), fault trace from Vallage et al. (2016), epicenter from Barnhart et al. (2014).

fail in shallow coseismic slip prediction and resulting in the ~9% shallow slip deficit we measure for this segment. Such results also raise the question of the occurrence of SSD in geometrical complexities.

Nonetheless, we see on average no shallow slip deficit for the Balochistan earthquake (Figure 15). We suggest that the absence of SSD may be related to the earthquake's larger magnitude compared to the set of earthquakes (Mw 6.5–7.5) that were previously reported to show shallow slip deficit. Indeed, some other large strike-slip earthquakes also show no shallow slip deficit, such as the 2001 Mw 7.8 Kokoxili (Lasserre et al., 2005; Ozacar, 2004) or the 2002 Mw 7.9 Denali (Elliott et al., 2007; Ozacar, 2004) earthquakes. These earthquakes are all earthquakes with a magnitude greater than 7.5. Conversely, the 1992 Mw 7.3 Landers (Fialko, 2004; Gombert et al., 2017; Xu et al., 2016), the 1997 Mw 7.2 Zirkuh (Sudhaus & Jónsson, 2011), the 1999 Mw 7.1 Hector Mine (Jónsson et al., 2002; Simons et al., 2002; Xu et al., 2016), the 2003 Mw 6.5 Bam (Fialko et al., 2005; Motagh et al., 2006; Wang et al., 2004), and the 2010 Mw 7.2 El

Mayor-Cucapah (Huang et al., 2017; Xu et al., 2016) earthquakes, which are smaller in magnitude, all seem to exhibit shallow slip deficit to some extent (Figure 14). Absence of shallow slip deficit for the 2015 Mw 7.2 Murghab earthquake (Sangha et al., 2017), however, indicates that even in this range of magnitude, SSD is not systematic. Thus, we suggest that this difference between very large strike-slip earthquakes, with magnitude about ~7.5 or above, and events with magnitude closer to 7 + rests in the fact that largest events are rupturing the entire thickness of the brittle crust to achieve such large magnitude. Smaller events, although they usually reach the ground surface as well, do not saturate the entire seismogenic thickness with slip, ending up with less slip toward the surface compared to zones closer to the middle depth of rupture patches. Confirming whether shallow slip deficit is related to the magnitude will certainly require more large strike-slip earthquakes to be recorded and modeled in order to see a clearer statistical pattern.

### 6.2. Segmentation and Barriers (Highlighted by the Balochistan Earthquake)

Earthquake rupture processes are commonly described in terms of barriers that can act as stoppers or as initiators of the earthquake rupture (Aki, 1979) and therefore delineate the ruptures (King & Nabelek, 1985). Along the rupture itself, high variations in the slip can be found and imputed to strong persistent geometric barriers separating the fault segments (Klinger et al., 2006). Two kinds of barrier can be distinguished: The geometric barriers are associated with locations where the orientation of a failure surface changes, while the relaxation barriers are characterized with low stress areas (King, 1986). On that basis, and with the help of the surface data, our modeled fault geometry, and the inferred slip distribution, we can formulate several hypotheses for the Balochistan earthquake about the role of fault sections along of the rupture, the unilateral propagation away from the Chaman Fault System, the rupture terminations, and the dominant strike-slip kinematics. We focus only on the first order features of our results that we believe more robust than small-scale details.

Despite some variations along the fault, the strike-slip component for the Balochistan rupture shows a quite continuous and smooth slip distribution (Figure 5) compared to other earthquakes such as the 2001 Mw 7.8 Kokoxili earthquake (Klinger et al., 2006). In our case, the segmentation does not stand out in the slip curves (Figure 5) or in the slip model (Figure 10) despite our effort to reproduce accurately the fault geometry.

Still, two barriers can be defined at each end of the rupture. At the northern extremity of the rupture, the inversion shows little slip propagating north of the epicenter, with no interaction with the Ornach-Nal, Chaman, or Ghazaband faults (Figure 10). Creep has however been observed on the northern part of the Hoshab fault both before (Fattahi et al., 2015) and after the earthquake (Peterson et al., 2018), suggesting that this part of the fault behaves as a relaxation barrier, characterized by low stress, which might impede further northward propagation. Creep on the northern part of the Hoshab fault could also have had an effect on the southern part of the Hoshab fault. The southern part is locked and continuous creep on the northern section could indeed transfer stress to the southern sections (pink arrows in Figure 16), hence inducing a long-term loading of this section and explaining the occurrence of the 2013 earthquake. Such phenomenon has already been suggested to explain large accumulations of stress that lead to the occurrence of great earthquakes such as the 1857 M 8 Fort Tejon earthquake (Rosen et al., 1998). Moreover, the area where the main Mw 6.8 aftershock took place was probably loaded by both the creep and the 2013 event since it occurred in the area in between (Figure 16), where neither creep nor coseismic slip have been detected.

At the southern tip of the fault, the dip analysis (gray curve in Figure 8d) and the non-linear inversion (violet curve in Figure 8d) both show a steepening of the fault. This steepening is likely resulting from the fact that toward its southern end, the Hoshab fault becomes parallel to the main thrust structures forming the accretionary wedge of the Makran subduction. Hence, as the wedge propagates southward though time, any thrust sliver located northward of the frontal wedge will progressively steepen, including the Hoshab fault. While the rupture is propagating southwestward along a structure which is less and less well oriented for strike-slip motion, it also encounters a structure that is steeper, making reverse motion more difficult as well. Thus, along the last segment, the rupture leaves the main topographic front corresponding to the long-term fault to propagate southward through Quaternary deposits along a direction more prone to strike-slip (Vallage et al., 2016). At the surface (Figure 5a), the last segment shows a dramatic drop of the coseismic slip at the surface, going from 7 m to 0 on a distance of ~10 km only. Eventually, the increasing distance of the fault from the plate boundary, the growing obliquity to the CFS and the more complex structure with changes in both the rupture orientation and dip may have induced conditions that are increasingly

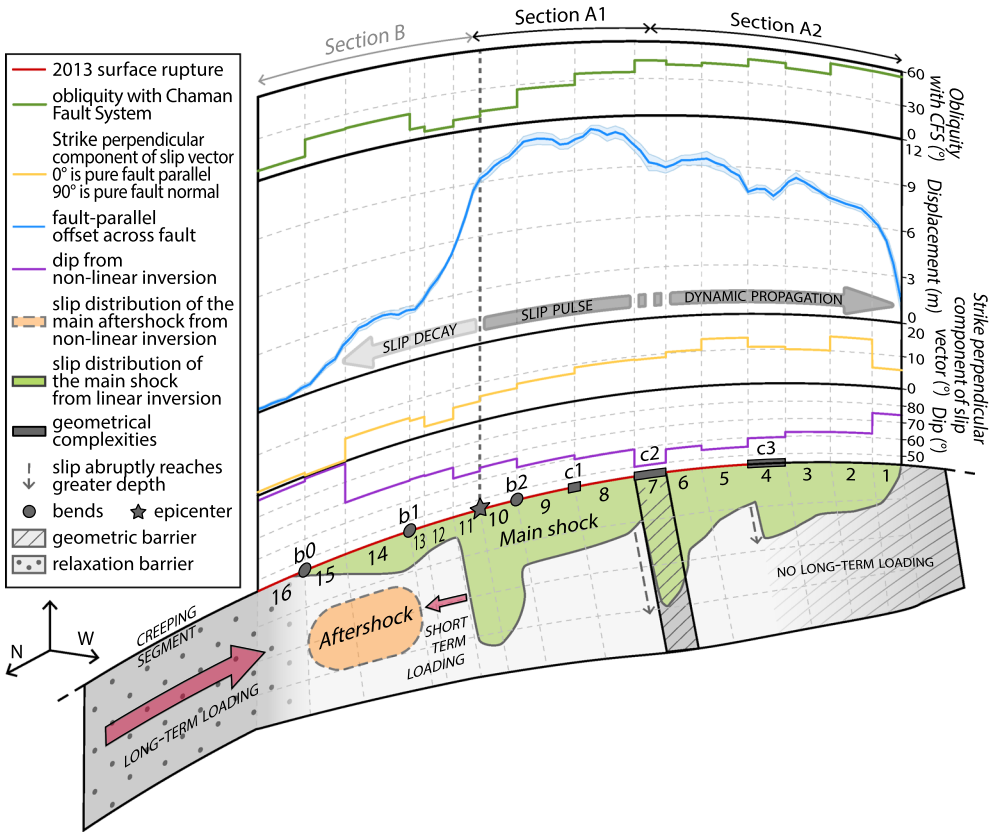


**Figure 16.** Interpretation of the Balochistan earthquake and summary of the main results. Blue curve shows the fault-parallel offset across the fault measured from surface data. Violet curve represents the dip obtained by non-linear inversion. Green curve shows the obliquity of the Hoshab fault with respect to the Chaman Fault System. Yellow curve represents the compression that we define as the difference between the fault azimuth and the projected rake on the surface for each fault segment (0° = pure fault parallel motion, 90° = pure reverse motion). Green and orange shapes stand for the area of coseismic and aftershock slip respectively. Red curve depicts the surface rupture with the epicenter (gray star), complexities (gray boxes) and bends (gray dots). Gray arrows show the slip directivity and interpretation in terms of rupture propagation and fault sections. Barriers fall in two categories: Geometric barriers (dashed boxes), where the rupture orientation changes, and the structural features become more complex; and relaxation barriers (dotted boxes) characterized by low stress values.

unfavorable to maintain the rupture itself, suggesting the last segment of the rupture may also be considered as a geometric barrier.

Moreover, a clear change in the kinematics occurs when the rupture propagates through the complexity C2 (location in Figure 4b). At the surface, slip is almost constantly increasing before the complexity, while it starts to slowly decrease after having broken the complexity, before finally terminating abruptly (Figures 5a and blue curve in Figure 16). At depth, C2 matches with a location where slip abruptly reaches a greater depth as the rupture propagates across the complexity (Figure 10, represented by dashed arrows in Figure 16). C2 also coincides with the location where the fault dip is shallowest (52°, Figure 5 and violet curve in Figure 16). On a large scale, it is also concordant with the area from which the strike-slip amplitude decreases whereas the reverse slip increases in the slip distribution (Figure 10). C2 thus seems to be a significant relay regarding both the fault geometry and the earthquake kinematics. In that perspective, we can define the relay C2 as a geometric barrier that separates two fault sections south of the epicenter. The first section (A1) goes from the epicenter to C2, and the second section (A2) dwells from C2 to the rupture termination (Figure 16). C2 thus separates both sections and currently corresponds to the location of transition from the Chaman strike-slip Fault System to the thrust structures of the accretionary prism. The fault geometry being unstable in the vicinity of the triple junction, this transition may have moved through time.

Furthermore, compared to other Mw 7 + strike-slip earthquakes for which we have a slip distribution along the strike of the fault, the slip to length ratio is much higher for the Balochistan earthquake. With a mean slip ($\bar{u}$) over 6 m for a distance (L) of almost 220 km, this earthquake represents an outlier when regarding the scaling laws established by Scholz in 1982 and Bodin and Brune in 1996 (Figure S24). This suggests that the stress drop ?σ, was higher during the Balochistan earthquake than for most of strike-slip earthquakes documented so far. Moreover, when the rupture reaches the complexity C2, the coseismic slip is at its peak, leading to a high stress drop in this area. We suspect this stress drop would then be high enough to break the complexity C2. Besides, the slow decrease of slip starting after C2 (blue curve in Figure 16) we observe on the second section (A2) would also be consistent with a strong dynamic component related to the high stress drop. In that perspective, we can infer that the coseismic slip was strong enough to attain a sufficiently high shear stress that allowed this section to slip even if it was not necessarily close to failure. The high stress drop would finally explain both this self-sustaining aspect of section A2 and the maintaining of a major strike-slip component on a fault that used to accommodate reverse motion during its past geological history (Lawrence et al., 1981; Platt et al., 1988).

Finally, the Balochistan earthquake is a hint for the existence of events with extreme surface slip, large stress drop and long recurrence time (Zhou et al., 2015) and points out the specific challenge to properly assess the hazard associated to such earthquakes.

## Data Availability Statement

Data associated to this research are available at https://doi.org/10.5281/zenodo.3653892 (geodetic data, 3-D solution, slip curves, fault segments location, dip estimates from non-linear inversion, and slip distribution from linear inversion).

**Acknowledgments**

Part of this work was supported by CNES TOSCA Program. TerraSAR-X data were provided by DLR (German Space Agency) under the Support to Science Initiative (proposal GEO2125). We thank DLR for synchronizing TerraSAR-X ScanSAR acquisitions, which otherwise would have been improper for interferometry. We thank the Canadian Space Agency (CSA) for programming the RADARSAT satellite and providing data crucial to this work. We thank Y. Gaudemer, R. Jolivet, A. Vallage, and N. Yague-Martinez for fruitful discussions. Numerical computations were partly performed on the S-CAPAD platform, IPGP, France. This is Institut de Physique du Globe de Paris (IPGP) Contribution Number 4112.

## References

Ader, T., Avouac, J.-P., Liu-Zeng, J., Lyon-Caen, H., Bollinger, L., Galetzka, J., et al. (2012). Convergence rate across the Nepal Himalaya and interseismic coupling on the Main Himalayan Thrust: Implications for seismic hazard. *Journal of Geophysical Research*, *117*, B04403. http://doi.org/10.1029/2011JB009071

Aki, K. (1979). Characterization of barriers on an earthquake fault. *Journal of Geophysical Research*, *84*(B11), 6140–6148. http://doi.org/10.1029/jb084ib11p06140

Ambraseys, N., & Bilham, R. (2003). Earthquakes and associated deformation in northern Baluchistan. *Bulletin of the Seismological Society of America*, *74*(2), 107–123. http://doi.org/10.1785/gssrl.74.2.107

Avouac, J.-P., Ayoub, F., Wei, S., Ampuero, J.-P., Meng, L., Leprince, S., et al. (2014). The 2013, Mw 7.7 Balochistan earthquake, energetic strike-slip reactivation of a thrust fault. *Earth and Planetary Science Letters*, *391*(C), 128–134. http://doi.org/10.1016/j.epsl.2014.01.036

Barnhart, W. D., Briggs, R. W., Reitman, N. G., Gold, R. D., & Hayes, G. P. (2015). Evidence for slip partitioning and bimodal slip behavior on a single fault: Surface slip characteristics of the 2013 Mw 7.7 Balochistan, Pakistan earthquake. *Earth and Planetary Science Letters*, *420*(C), 1–11. http://doi.org/10.1016/j.epsl.2015.03.027

Barnhart, W. D., Gold, R. D., Shea, H. N., Peterson, K. E., Briggs, R. W., & Harbor, D. J. (2019). Vertical coseismic offsets derived from high-resolution stereogrammetric DSM differencing: The 2013 Baluchistan, Pakistan Earthquake. *Journal of Geophysical Research: Solid Earth.*, *124*, 6039–6055. http://doi.org/10.1029/2018JB017107

Barnhart, W. D., Hayes, G. P., Briggs, R. W., Gold, R. D., & Bilham, R. (2014). Ball-and-socket tectonic rotation during the 2013 Mw 7.7 Balochistan earthquake. *Earth and Planetary Science Letters*, *403*(C), 210–216. http://doi.org/10.1016/j.epsl.2014.07.001

Bilham, R., Lodi, S., Hough, S., Bukhary, S., Khan, A. M., & Rafeeqi, S. F. A. (2007). Seismic hazard in Karachi, Pakistan: Un-certain past, uncertain future. *Seismological Research Letters*, *78*(6), 601–613. http://doi.org/10.1785/gssrl.78.6.601

Bodin, P., & Brune, J. N. (1996). On the scaling of slip with rupture length for shallow strike-slip earthquakes: Quasi-static models and dynamic rupture propagation. *Bulletin of the Seismological Society of America*, *86*(5), 1292–1299.

Byrne, D. E., Sykes, L. R., & Davis, D. M. (1992). Great thrust earthquakes and aseismic slip along the plate boundary of the Makran subduction zone. *Journal of Geophysical Research*, *97*(B1), 449–478. http://doi.org/10.1029/91JB02165

Choi, J.-H., Klinger, Y., Ferry, M., Ritz, J.-F., Kurtz, R., Rizza, M., et al. (2018). Geologic inheritance and earthquake rupture processes: The 1905 M ≥ 8 Tsetserleg-Bulnay strike-slip earthquake sequence, Mongolia. *Journal of Geophysical Research: Solid Earth*, *123*, 1925–1953. http://doi.org/10.1002/2017JB013962

DeMets, C., Gordon, R. G., & Argus, D. F. (2010). Geologically current plate motions. *Geophysical Journal International*, *181*(1), 1–80. http://doi.org/10.1111/j.1365-246X.2009.04491.x

Doin, M.-P., Guillaso, S., Jolivet, R., Lasserre, C., Lodge, F., Ducret, G., & Grandin, R. (2011). Presentation of the small baseline NSBAS processing chain on a case example: The Etna deformation monitoring from 2003 to 2010 using Envisat data. pages 3434–3437.

Dolan, J. F., & Haravitch, B. D. (2014). How well do surface slip measurements track slip at depth in large strike-slip earthquakes? The importance of fault structural maturity in controlling on-fault slip versus off-fault surface deformation. *Earth and Planetary Science Letters*, *388*, 38–47. http://doi.org/10.1016/j.epsl.2013.11.043

Elliott, J. L., Freymueller, J. T., & Rabus, B. (2007). Coseismic deformation of the 2002 Denali fault earthquake: Contributions from synthetic aperture radar range offsets. *Journal of Geophysical Research*, *112*, B06421. http://doi.org/10.1029/2006JB004428

Ellouz-Zimmermann, N., Deville, E., Mueller, C., Lallemant, S., Subhani, A. B., & Tabreez, A. R. (2007). Impact of sedimentation on convergent margin tectonics: Example of the Makran accretionary prism (Pakistan).

Fattahi, H., Amelung, F., Chaussard, E., & Wdowinski, S. (2015). Coseismic and postseismic deformation due to the 2007 M5.5 Ghazaband fault earthquake, Balochistan, Pakistan. *Geophysical Research Letters*, *42*, 3305–3312. http://doi.org/10.1002/2015GL063686

Fialko, Y. (2004). Probing the mechanical properties of seismically active crust with space geodesy: Study of the coseismic deformation due to the 1992 Mw 7.3 Landers (southern California) earthquake. *Journal of Geophysical Research*, *109*, B03307-1. http://doi.org/10.1029/2003JB002756

Fialko, Y., Sandwell, D. T., Simons, M., & Rosen, P. A. (2005). Three-dimensional deformation caused by the Bam, Iran, earthquake and the origin of shallow slip deficit. *Nature*, *435*(7040), 295–299. http://doi.org/10.1038/nature03425

Fialko, Y., Simons, M., & Agnew, D. (2001). The complete (3-D) surface displacement field in the epicentral area of the 1999 Mw 7.1 Hector Mine earthquake, California, from space geodetic observations. *Geophysical Research Letters*, *28*(16), 3063–3066. https://doi.org/10.1029/2001GL013174

Gold, R. D., Reitman, N. G., Briggs, R. W., Barnhart, W. D., Hayes, G. P., & Wilson, E. (2015). On- and off-fault deformation associated with the September 2013 Mw 7.7 Balochistan earthquake: Implications for geologic slip rate measurements. *Tectonophysics*, *660*, 65–78. http://doi.org/10.1016/j.tecto.2015.08.019

Gombert, B., Duputel, Z., Jolivet, R., Doubre, C., Rivera, L., & Simons, M. (2017). Revisiting the 1992 Landers earthquake: A Bayesian exploration of co-seismic slip and off-fault damage. *Geophysical Journal International*, *212*(2), 839–852. http://doi.org/10.1093/gji/ggx455

Grandin, R. (2015, March). Interferometric processing of SLC Sentinel-1 TOPS data. In FRINGE'15: Advances in the science and applications of SAR interferometry and Sentinel-1 InSAR workshop, Frascati, Italy, 23-27 March 2015.

Grandin, R., Socquet, A., Binet, R., Klinger, Y., Jacques, E., De Chabalier, J.-B., et al. (2009). September 2005 Manda Hararo-Dabbahu rifting event, Afar (Ethiopia): Constraints provided by geodetic data. *Journal of Geophysical Research*, *114*, B08404. http://doi.org/10.1029/2008JB005843

Holzner, J., & Bamler, R. (2002). Burst-mode and ScanSAR interferometry. *IEEE Transactions on Geoscience and Remote Sensing*, *40*(9), 1917–1934. http://doi.org/10.1109/TGRS.2002.803848

Huang, M.-H., Fielding, E. J., Dickinson, H., Sun, J., Gonzalez-Ortega, A. J., Freed, A. M., & Bürgmann, R. (2017). Fault geometry inversion and slip distribution of the 2010 M w7.2 El Mayor-Cucapah Earthquake from geodetic data. *Journal of Geophysical Research: Solid Earth*, *122*, 607–621. http://doi.org/10.1002/2016JB012858

Jolivet, R., Duputel, Z., Riel, B., Simons, M., Rivera, L., Minson, S. E., et al. (2014). The 2013 Mw 7.7 Balochistan earthquake: Seismic potential of an accretionary wedge. *Bulletin of the Seismological Society of America*, *104*(2), 1020–1030. http://doi.org/10.1785/0120130313

Jónsson, S., Zebker, H., Segall, P., & Amelung, F. (2002). Fault slip distribution of the 1999 Mw 7.1 Hector mine, California, earthquake, estimated from satellite radar and GPS measurements. *Bulletin of the Seismological Society of America*, *92*(4), 1377–1389. https://doi.org/10.1785/0120000922

Kaneko, Y., & Fialko, Y. (2011). Shallow slip deficit due to large strike-slip earthquakes in dynamic rupture simulations with elasto-plastic off-fault response. *Geophysical Journal International*, *186*(3), 1389–1403. http://doi.org/10.1111/j.1365-246X.2011.05117.x

Kim, S.-J., Koh, K., Boyd, S., & Gorinevsky, D. (2009). L1 trend filtering. *SIAM Review*, *51*(2), 339–360. http://doi.org/10.1137/070690274

King, G. C. P. (1986). Speculations on the geometry of the initiation and termination processes of earthquake rupture and its relation to morphology and geological structure. *Pure and Applied Geophysics*, *124*(3), 567–585. http://doi.org/10.1007/bf00877216

King, G. C. P., & Nabelek, J. (1985). Role of fault bends in the initiation and termination of earthquake rupture. *Science*, *228*(4702), 984–987. http://doi.org/10.1126/science.228.4702.984

Klinger, Y. (2010). Relation between continental strike-slip earthquake segmentation and thickness of the crust. *Journal of Geophysical Research*, *115*, B07306. http://doi.org/10.1029/2009JB006550

Klinger, Y., Michel, R., & King, G. C. P. (2006). Evidence for an earthquake barrier model from Mw ⁄7.8 Kokoxili (Tibet) earthquake slip-distribution. *Earth and Planetary Science Letters*, *242*(3–4), 354–364. http://doi.org/10.1016/j.epsl.2005.12.003

Kukowski, N., Schillhorn, T., Flueh, E. R., & Huhn, K. (2000). Newly identified strike-slip plate boundary in the northeastern Arabian Sea. *Geology*, *28*(4), 355–358. https://doi.org/10.1130/0091-7613(2000)28%3C355:NISPBI%3E2.0.CO;2

Lasserre, C., Peltzer, G., Crampé, F., Klinger, Y., Van der Woerd, J., & Tapponnier, P. (2005). Coseismic deformation of the 2001 Mw = 7.8 Kokoxili earthquake in Tibet, measured by synthetic aperture radar interferometry. *Journal of Geophysical Research*, *110*, B12408. http://doi.org/10.1029/2004JB003500

Lawrence, R. D., Yeats, R. S., & Khan, S. H. (1981). Thrust and strike slip fault interaction along the Chaman transform zone, Pakistan. *Thrust and Nappe Tectonics. The Geological Society of London*, *9*(1), 363–370. https://doi.org/10.1144/GSL.SP.1981.009.01.33

Lawson, C. L., & Hanson, R. J. (1974). *Solving least squares problems*. Englewood Cliffs: Prentice-Hall.

Leprince, S., Barbot, S., Ayoub, F., & Avouac, J.-P. (2007). Automatic and precise orthorectification, coregistration, and subpixel correlation of satellite images, application to ground deformation measurements. *IEEE Transactions on Geoscience and Remote Sensing*, *45*(6), 1529–1558. http://doi.org/10.1109/TGRS.2006.888937

Liang, C., Zeng, Q., Jia, J., Jiao, J., & Cui, X. (2013). ScanSAR interferometric processing using existing standard InSAR software for measuring large scale land deformation. *Computers and Geosciences*, *51*(C), 439–448. http://doi.org/10.1016/j.cageo.2012.08.011

Lohman, R. B., & Simons, M. (2005). Some thoughts on the use of InSAR data to constrain models of surface deformation: Noise structure and data downsampling. *Geochemistry, Geophysics, Geosystems*, *6*, Q01007. http://doi.org/10.1029/2004GC000841

Malavieille, J. (1984). Modélisation experimentale des chevauchements imbriqués: Application aux chaines de montagnes. *Bulletin De La Société Géologique De France*, *7*(1), 129–138.

Marchandon, M., Vergnolle, M., Sudhaus, H., & Cavalié, O. (2018). Fault geometry and slip distribution at depth of the 1997 Mw 7.2 Zirkuh earthquake: Contribution of near-field displacement data. *Journal of Geophysical Research: Solid Earth*, *123*, 1904–1924. http://doi.org/10.1002/2017JB014703

Massonnet, D., & Feigl, K. L. (1998). Radar interferometry and its application to changes in the Earth's surface. *Reviews of Geophysics*, *36*(4), 441–500. https://doi.org/10.1029/97RG03139

Menke, W. (1989). *Geophysical data analysis: Discrete inverse theory*, *International Geophysics Series*, (Rev.ed. ed.). New York: Academic Press.

Michel, R., & Avouac, J.-P. (1999). Measuring ground displacements from SAR amplitude images: Application to the Landers earthquake. *Geophysical Research Letters*, *26*(7), 875–878. https://doi.org/10.1029/1999GL900138

Motagh, M., Klotz, J., Tavakoli, F., Djamour, Y., Arabi, S., Wetzel, H.-U., & Zschau, J. (2006). Combination of precise leveling and InSAR data to constrain source parameters of the Mw = 6.5, 26 December 2003 Bam Earthquake. *Pure and Applied Geophysics*, *163*(1), 1–18. http://doi.org/10.1007/s00024-005-0005-y

Okada, Y. (1992). Internal deformation due to shear and tensile faults in a halfspace. *Bulletin of the Seismological Society of America*, *82*(2), 1018–1040.

Ozacar, A. A. (2004). The 2002 Denali Fault and 2001 Kunlun Fault Earthquakes: Complex rupture processes of two large strike-slip events. *Bulletin of the Seismological Society of America*, *94*(6B), S278–S292. http://doi.org/10.1785/0120040604

Peterson, K. E., Barnhart, W. D., & Li, S. (2018). Viscous accretionary prisms: Viscoelastic relaxation of the Makran accretionary prism following the 2013 Baluchistan, Pakistan Earthquake. *Journal of Geophysical Research: Solid Earth*, *123*, 10,107–10,123. http://doi.org/10.1029/2018JB016057

Platt, J. P., Leggett, J. K., & Alam, S. (1988). Slip vectors and fault mechanics in the Makran Accretionary Wedge, southwest Pakistan. *Journal of Geophysical Research*, *93*(B7), 7955–7973. https://doi.org/10.1029/JB093iB07p07955

Radiguet, M., Cotton, F., Vergnolle, M., Campillo, M., Valette, B., Kostoglodov, V., & Cotte, N. (2011). Spatial and temporal evolution of a long term slow slip event: The 2006 Guerrero slow slip event. *Geophysical Journal International*, *184*(2), 816–828. https://doi.org/10.1111/j.1365-246X.2010.04866.x

Ragon, T., Sladen, A., & Simons, M. (2018). Accounting for uncertain fault geometry in earthquake source inversions – I: Theory and simplified application. *Geophysical Journal International*, *214*(2), 1174–1190. http://doi.org/10.1093/gji/ggy187

Reilinger, R. E., McClusky, S., Vernant, P., Lawrence, S., Ergintav, S., Cakmak, R., et al. (2006). GPS constraints on continental deformation in the Africa-Arabia-Eurasia continental collision zone and implications for the dynamics of plate interactions. *Journal of Geophysical Research*, *111*, B05411. http://doi.org/10.1029/2005JB004051

Rosen, P. A., Hensley, S., Peltzer, G., & Simons, M. (2004). Updated repeat orbit interferometry package released. *Eos Trans. AGU*, *85*(5), 47–47. http://doi.org/10.1029/2004EO050004

Rosu, A.-M., Pierrot-Deseilligny, M., Delorme, A., Binet, R., & Klinger, Y. (2014). Measurement of ground displacement from optical satellite image correlation using the free open-source software MicMac. *ISPRS Journal of Photogrammetry and Remote Sensing*, *100*, 48–59. http://doi.org/10.1016/j.isprsjprs.2014.03.002

Roth, A., Eineder, M., & Schättler, B. (2002). TerraSAR-X: A new perspective for applications requiring high resolution spaceborne SAR data. Presented at the Proceedings of the Joint ISPRS.

Sangha, S., Peltzer, G., Zhang, A., Meng, L., Liang, C., Lundgren, P., & Fielding, E. J. (2017). Fault geometry of 2015, Mw 7.2 Murghab, Tajikistan earthquake controls rupture propagation: Insights from InSAR and seismological data. *Earth and Planetary Science Letters*, *462*, 132–141. http://doi.org/10.1016/j.epsl.2017.01.018

Scholz, C. H. (1982). Scaling laws for large earthquakes: Consequences for physical models. *Bulletin of the Seismological Society of America*, *72*(1), 1–14.

Simons, M., Fialko, Y., & Rivera, L. (2002). Coseismic deformation from the 1999 Mw 7.1 Hector Mine, California, earthquake as inferred from InSAR and GPS observations. *Bulletin of the Seismological Society of America*, *92*(4), 1390–1402. https://doi.org/10.1785/0120000933

Simons, M., & Rosen, P. A. (2007). Interferometric synthetic aperture radar geodesy. *Treatise on Geophysics*, *3*, 391–446. https://doi.org/10.1016/B978-044452748-6/00059-6

Singh, D. D., & Gupta, H. K. (1980). Source dynamics of two great earthquakes of the Indian subcontinent: The Bihar-Nepal earthquake of January 15, 1934 and the Quetta earthquake of may 30, 1935. *Bulletin of the Seismological Society of America*, *70*(3), 757–773.

Sudhaus, H., & Jónsson, S. (2011). Source model for the 1997 Zirkuh earthquake (MW = 7.2) in Iran derived from JERS and ERS InSAR observations. *Geophysical Journal International*, *185*(2), 676–692. http://doi.org/10.1111/j.1365-246X.2011.04973.x

Szeliga, W., Bilham, R., Kakar, D. M., & Lodi, S. H. (2012). Interseismic strain accumulation along the western boundary of the Indian subcontinent. *Journal of Geophysical Research*, *117*, B08404. http://doi.org/10.1029/2011JB008822

Tarantola, A., & Valette, B. (1982). Generalized nonlinear inverse problems solved using the least squares criterion. *Reviews of Geophysics*, *20*(2), 219–232. https://doi.org/10.1029/RG020i002p00219

Thompson, T. B., & Meade, B. J. (2018). Topography and the shallow slip deficit inference. http://doi.org/10.31223/osf.io/puz84

Vallage, A., Klinger, Y., Grandin, R., Bhat, H. S., & Pierrot-Deseilligny, M. (2015). Inelastic surface deformation during the 2013 M w7.7 Balochistan, Pakistan, earthquake. *Geology*, *43*, 1079–1082. http://doi.org/10.1130/G37290.1

Vallage, A., Klinger, Y., Lacassin, R., Delorme, A., & Pierrot-Deseilligny, M. (2016). Geological structures control on earthquake ruptures: The Mw 7.7, 2013, Balochistan earthquake, Pakistan. *Geophysical Research Letters*, *43*, 10,155–10,163. https://doi.org/10.1002/2016GL070418

Wang, R., Xia, Y., Grosser, H., & Wetzel, H.-U. (2004). The 2003 Bam (SE Iran) earthquake: Precise source parameters from satellite radar interferometry. *Geophysical Journal International*, *159*(3), 917–922. https://doi.org/10.1111/j.1365-246X.2004.02476.x

Wells, D. L., & Coppersmith, K. J. (1994). New empirical relationships among magnitude, rupture length, rupture width, rupture area, and surface displacement. *Bulletin of the Seismological Society of America*, *84*(4), 974–1002.

Wright, T. J., Lu, Z., & Wicks, C. (2004). Constraining the slip distribution and fault geometry of the Mw 7.9, 3 November 2002, Denali fault earthquake with interferometric synthetic aperture radar and global positioning system data. *Bulletin of the Seismological Society of America*, *94*(6B), S175–S189. https://doi.org/10.1785/0120040623

Xu, X., Tong, X., Sandwell, D. T., Milliner, C. W. D., Dolan, J. F., Hollingsworth, J., et al. (2016). Refining the shallow slip deficit. *Geophysical Journal International*, *204*(3), 1843–1862. http://doi.org/10.1093/gji/ggv563

Yague-Martinez, N., Fielding, E. J., Haghshenas-Haghighi, M., Cong, X. Y., Motagh, M., Steinbrecher, U., et al. (2014). Ground displacement measurement of the 2013 M7.7 and M6.8 Balochistan Earthquake with TerraSAR-X ScanSAR data (pp. 950–953). IEEE. http://doi.org/10.1109/igarss.2014.6946583

Zhou, Y., Elliott, J. R., & Parsons, B. E. (2015). The 2013 Balochistan earthquake: An extraordinary or completely ordinary event? *Geophysical Research Letters*, *42*, 6236–6243. http://doi.org/10.1002/2015GL065096

Zhou, Y., Parsons, B. E., & Walker, R. T. (2018). Characterizing complex surface ruptures in the 2013 Mw 7.7 Balochistan Earthquake using three-dimensional displacements. *Journal of Geophysical Research: Solid Earth*, *123*, 10,191–10,211. http://doi.org/10.1029/2018JB016043

Zhou, Y., Walker, R. T., Elliott, J. R., & Parsons, B. E. (2016). Mapping 3D fault geometry in earthquakes using high-resolution topography: Examples from the 2010 El Mayor-Cucapah (Mexico) and 2013 Balochistan (Pakistan) earthquakes. *Geophysical Research Letters*, *43*, 3134–3142. http://doi.org/10.1002/2016GL067899

Zinke, R., Hollingsworth, J., & Dolan, J. F. (2014). Surface slip and off-fault deformation patterns in the 2013 M W7.7 Balochistan, Pakistan earthquake: Implications for controls on the distribution of near-surface coseismic slip. *Geochemistry, Geophysics, Geosystems*, *15*, 5034–5050. http://doi.org/10.1002/2014GC005538